Chapter 8

Solar flares

8.1 Basic concepts

A solar flare is a sudden realease of magnetic energy that has been stored in the field. Flares are associated with particle acceleration and heating. There have been many attempts to classify solar flares, but many of the classifications are outdated, mainly because they have been based on the outlook and appearance of events and not on the physical processes. The "impulsive – gradual" separation is still used, and it has worked best in describing energetic particle events. The "small – large" classification depends on the wavelength, but "confined – ejective" is still usuful because it describes plasma motions and also makes a difference between magnetic field configurations (if the field opens or not).

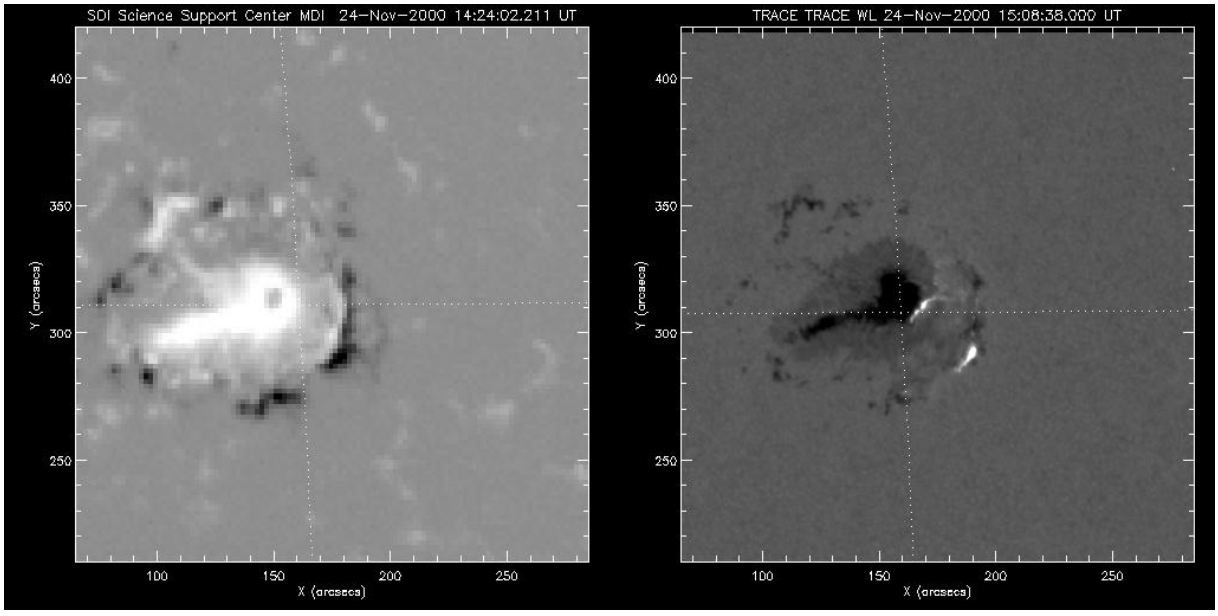

Figure 8.1: A solar flare is a sudden realease of magnetic energy, stored in the field. The earlier definition required an H-alpha brightening. The TRACE image on the right shows a two-ribbon flare observed in white light and the SOHO MDI image on the left shows the magnetic polarities and the field strength within the region. Eruptions often occur on the edges of sunspots, where the opposite polarity fields meet.

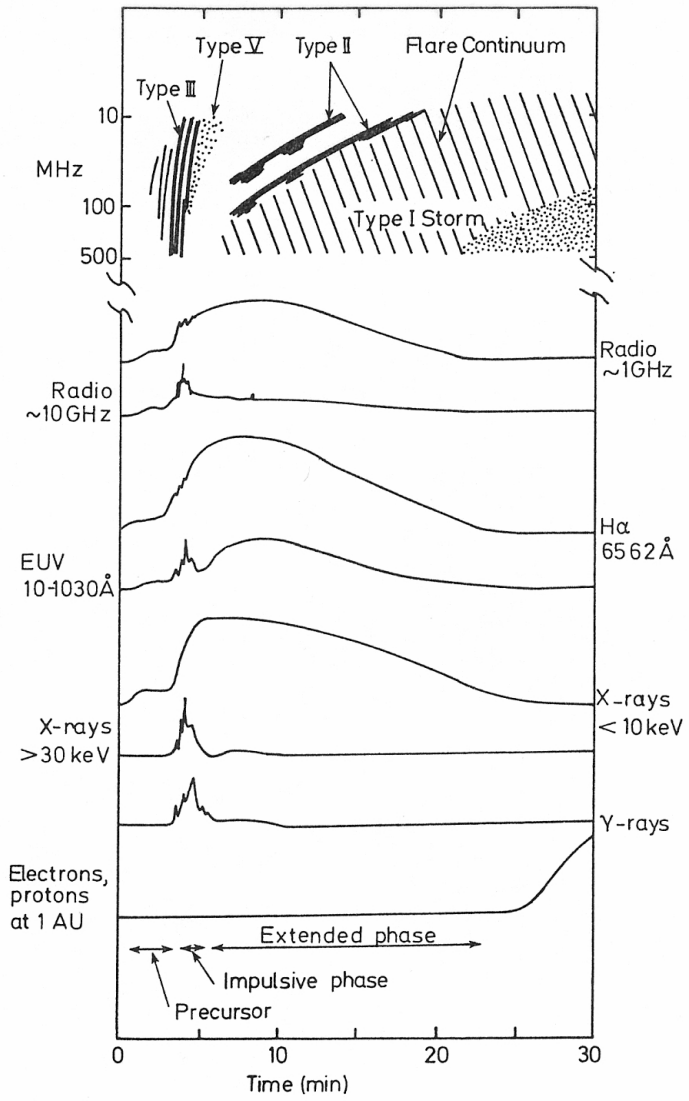

Fig. 4.1 – A schematic representation of the different phases of a typical solar flare as observed in electromagnetic and particle radiation. (Adapted from Kane 1974.)

Impulsive – Gradual

- Impulsive: Fast flux changes and non-thermal emission in hard X-rays and radio, may include a later thermal “tail” or “post-burst increase”
- Gradual: Almost purely thermal emission, hot plasma loops radiate thermal bremsstrahlung in soft X-rays and radio

Confined – Eruptive

- Depends whether magnetic fields open or not
- Diagnostics with radio type III emission (electron beams stream out along open magnetic field lines – or field lines stay closed and no type III bursts are observed)

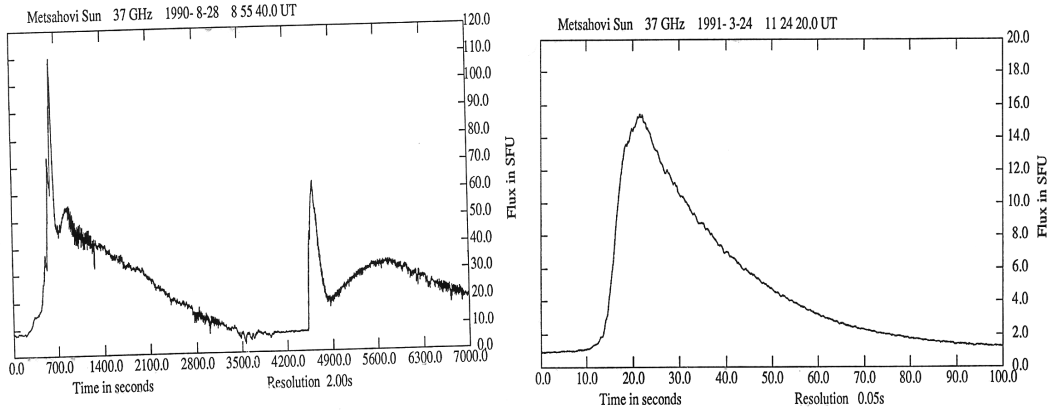

Figure 8.2: On the left: Impulsive burst + thermal tail. On the right: short impulsive burst without thermal emission (Metsähovi radio observations at 37 GHz).

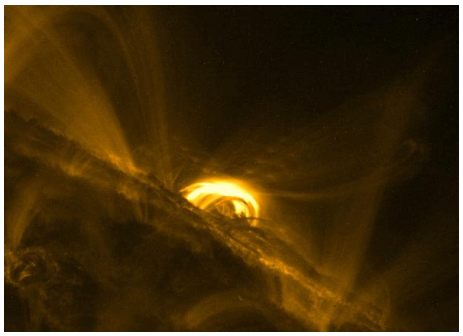

Figure 8.3: Flaring loop observed by TRACE at 171 Å.

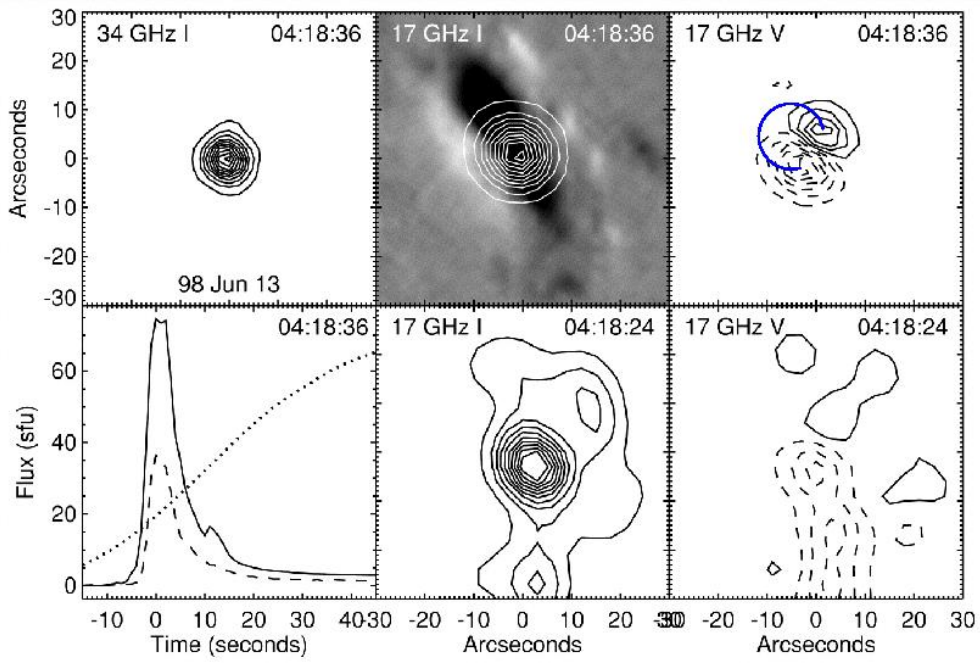

Figure 8.4: The 17 GHz emission (upper right plot; I=L+R, V=L-R) shows loop footpoints that have opposite polarization. The trapped particles are emitting gyrosynchrotron emission, and the direction of gyration is different at different loop ends. (Kundu et al., ApJ 547, 2001)

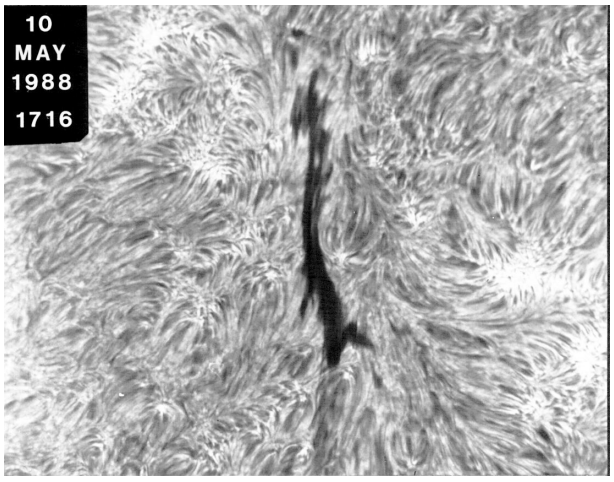

Figure 8.5: Filaments are cool and dense structures and they look dark in H_α as they are observed against the bright solar disk. The same happens at most radio wavelengths.

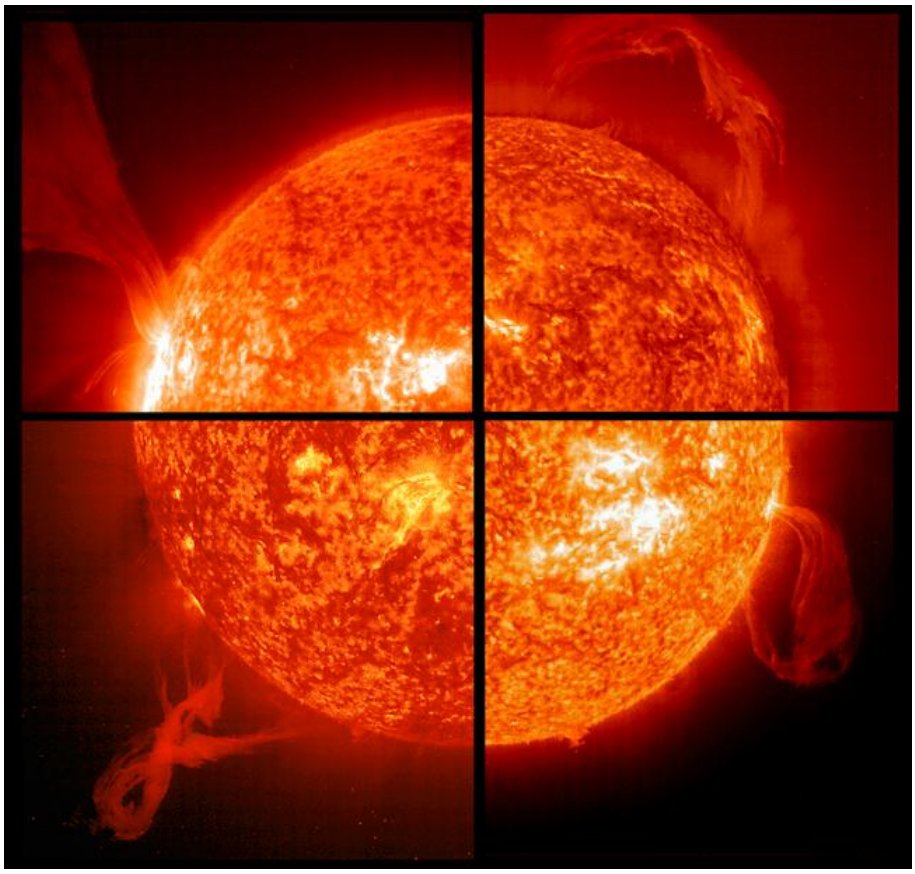

Figure 8.6: Filaments look bright when observed above the limb. Their appearances can be quite different (SOHO EIT, He II images).

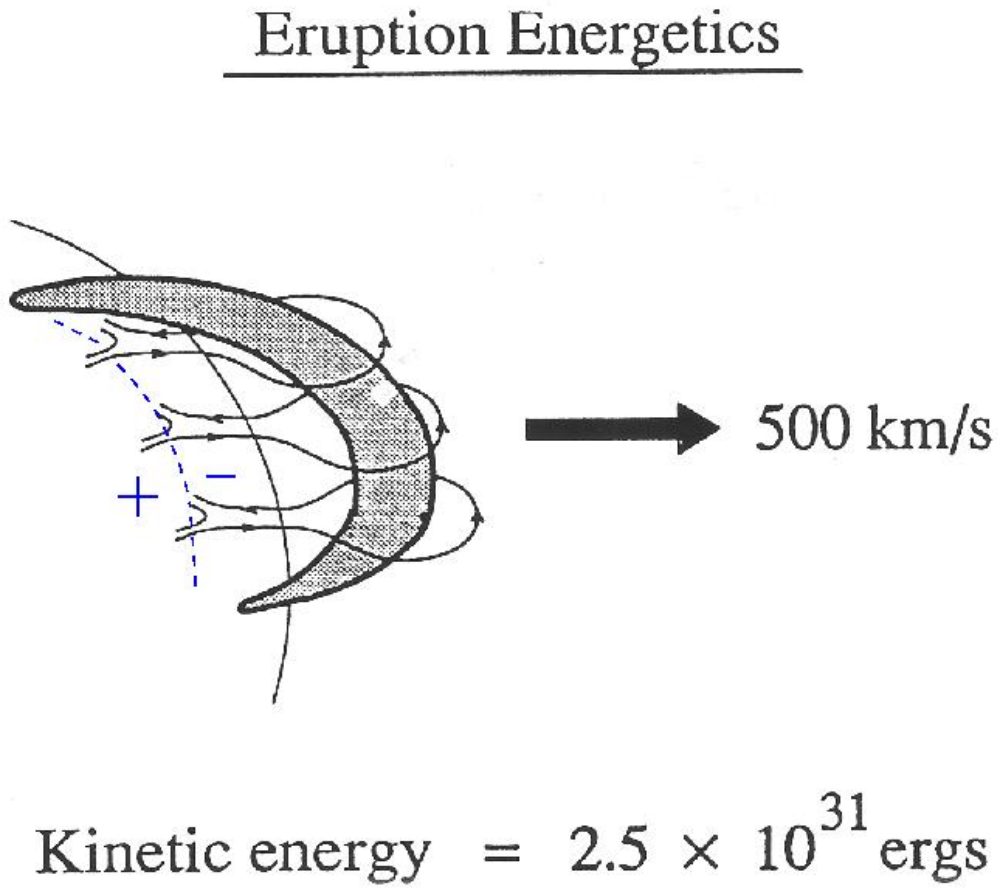

Figure 8.7: A filament "floats" in the solar atmosphere but is kept in place by magnetic field lines. Filaments are located above neutral lines, they are lines that separate oppositely polarized fields. If the oppositely directed fields reconnect below the filament, this may cause the filament to erupt. (From the MHD lectures by Terry Forbes)

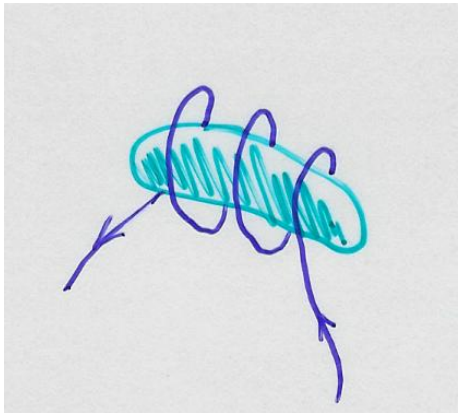

Figure 8.8: A flux rope scenario that is sometimes used for modeling filament eruptions - reconnecting field lines are now at the ends of the filament.

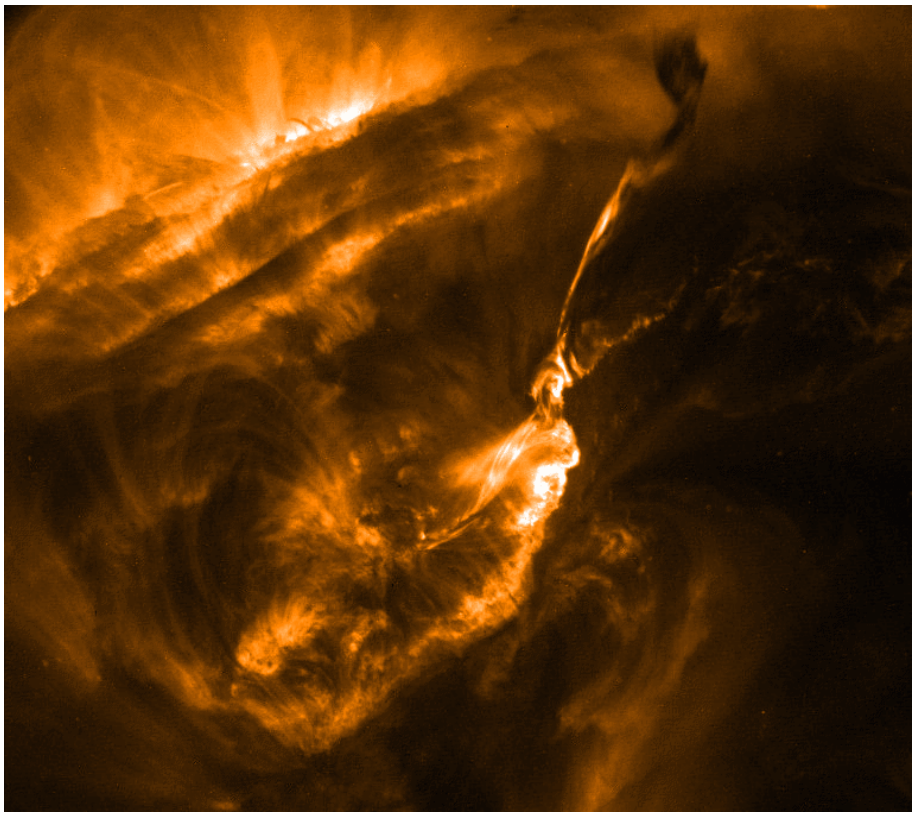

Figure 8.9: Filament eruptions are often (but not always) associated with flares. TRACE image shows bright regions at 1.5 MK temperature (more images at the TRACE web archive, by Karel Schrijver).

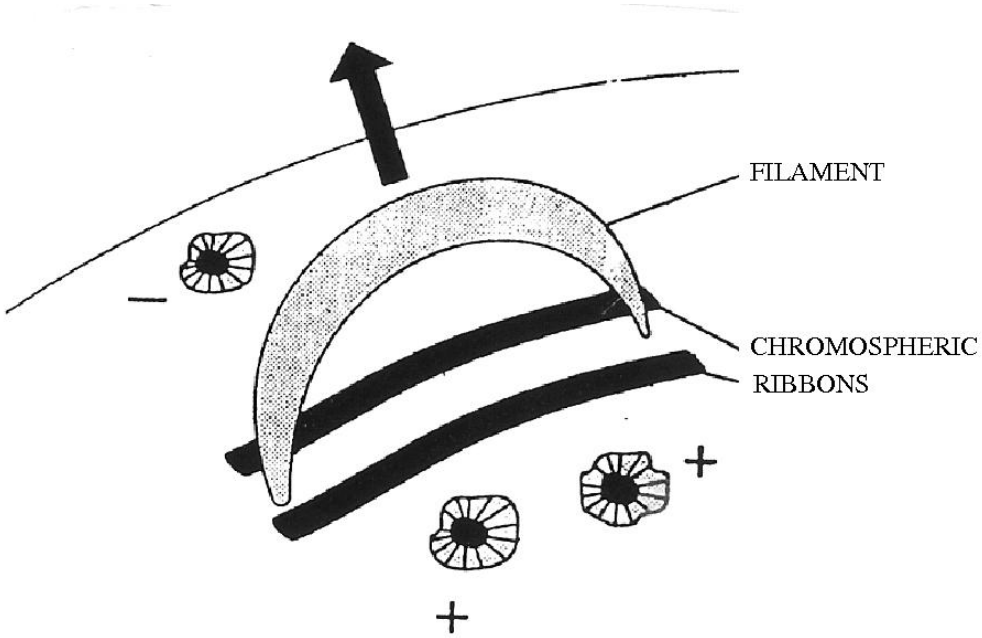

Figure 8.10: Filament eruption cartoon.

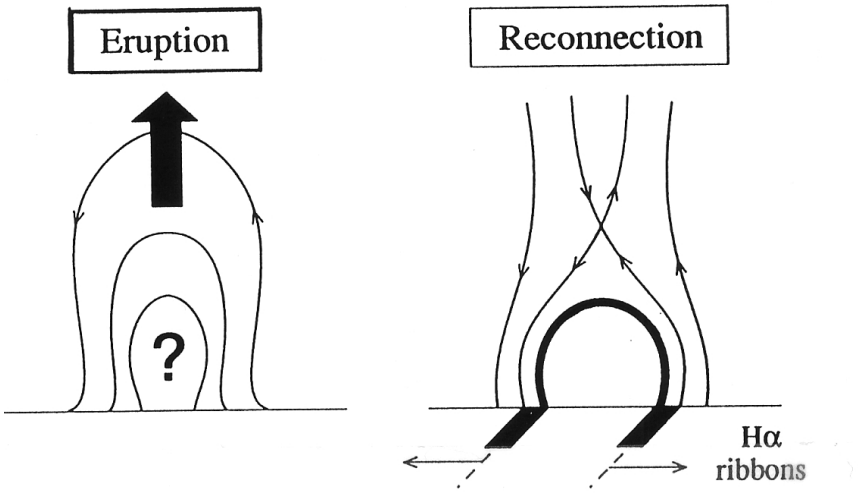

Figure 8.11: Eruption cartoon with a big question mark for trigger.

8.2 Flare models

Solar flare models have evolved from solenoids (Carmichael, 1963) to different types of reconnection scenarios (Sturrock 1966, Hirayama 1974, Kopp & Pneumann 1976) - hence the shortening CSHKP. The Grand Archive by Hugh Hudson contains practically all the available cartoons, see http://solarmuri.ssl.berkeley.edu/~hhudson/cartoons/overview.html

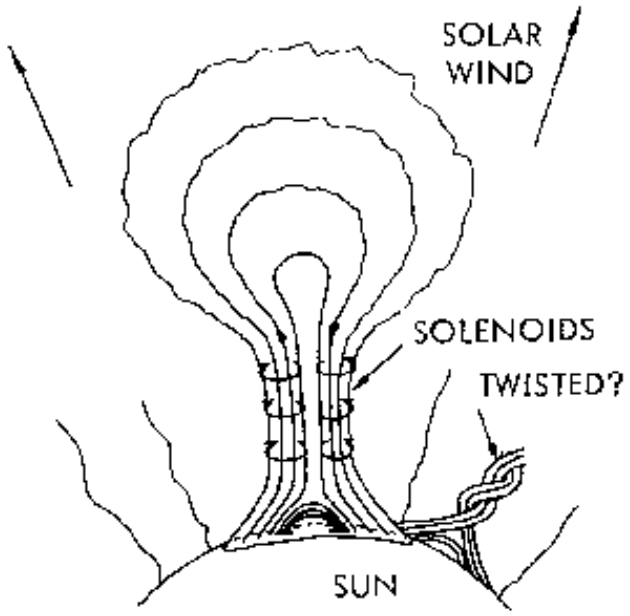

Figure 8.12: Development of flare models: Carmichael, 1960.

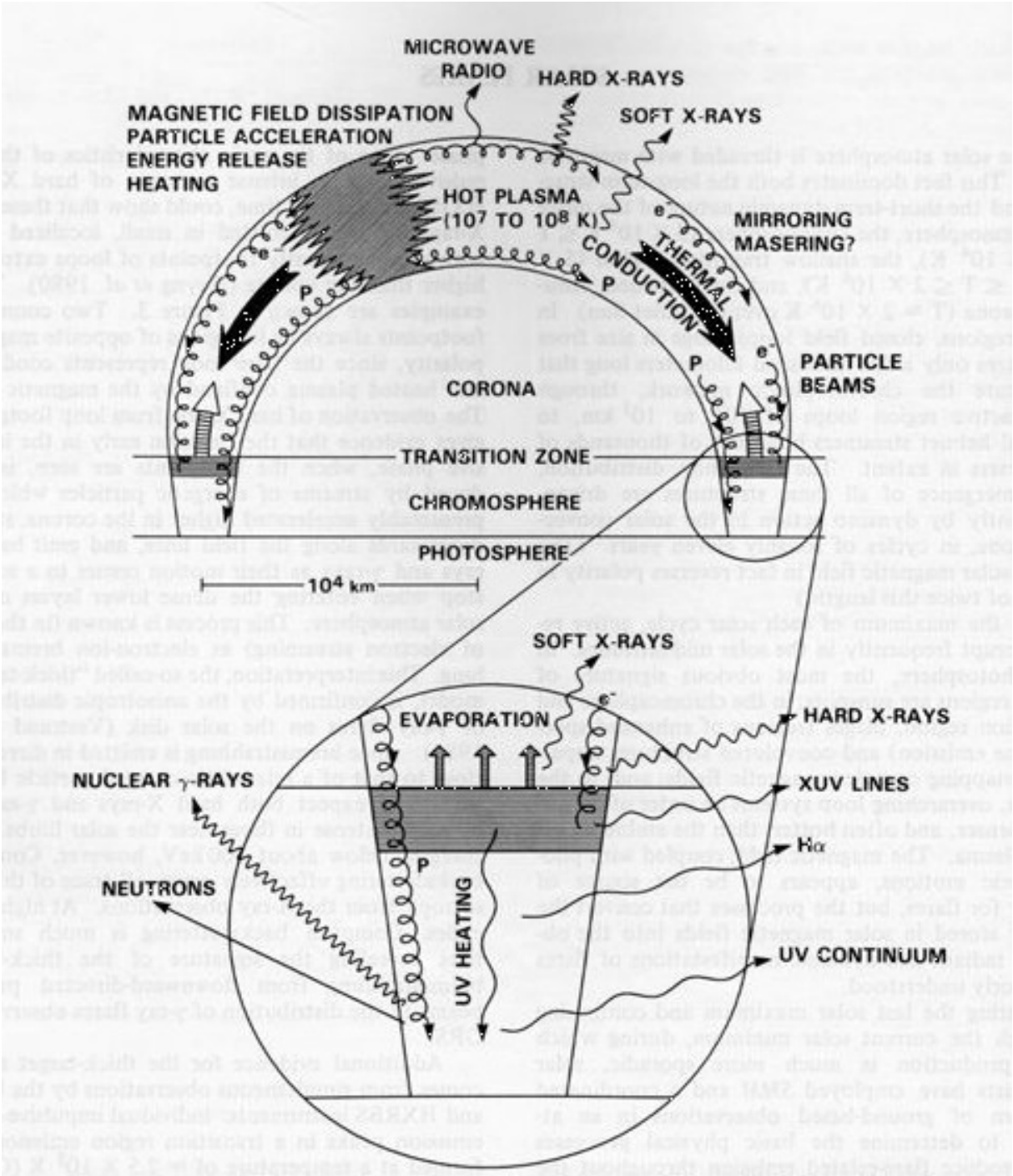

Figure 8.13: A simple model for a flare loop and associated emission (Gurman, 1987).

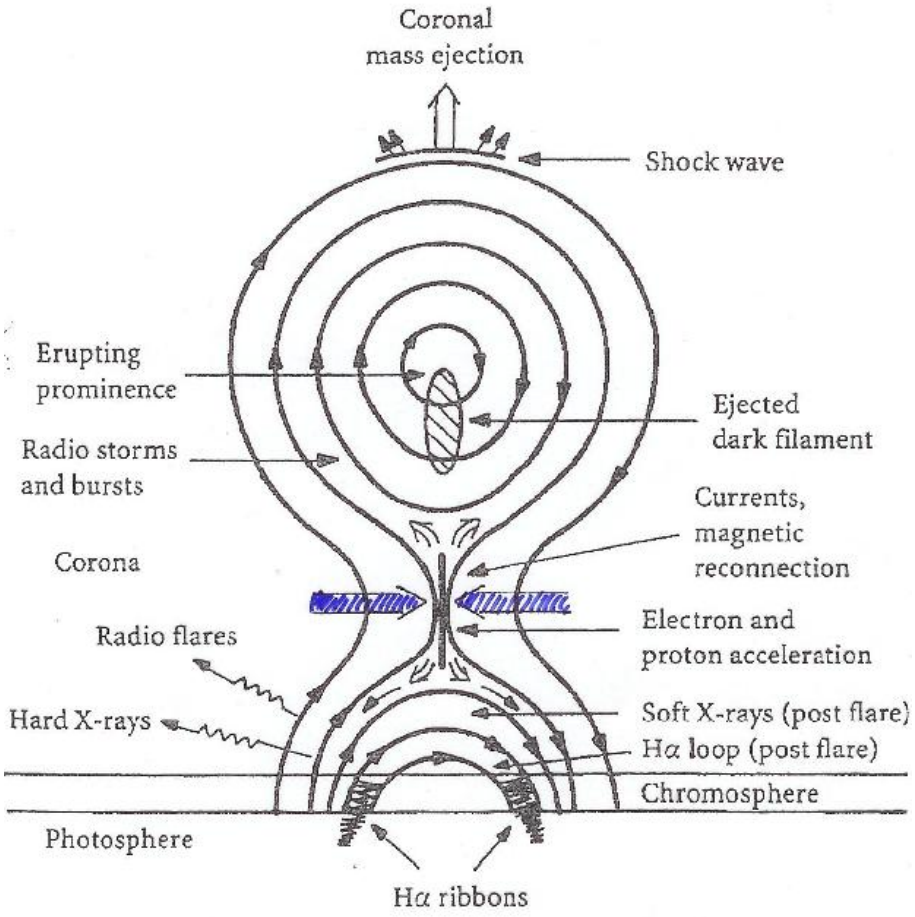

Figure 8.14: Filament eruption + flare in cross-section. This model also presents the connection between flares, filament eruptions, and coronal mass ejections. (K. Lang, 1995, copied from Kallenrode: Space Physics, 1998.)

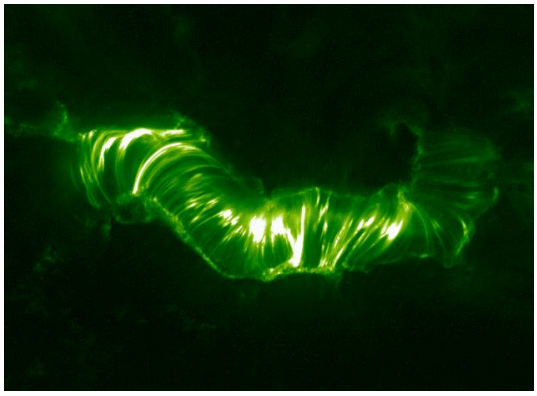

Figure 8.15: Post-flare loops form a rapidly cooling arcade of loops, in between the ribbons (TRACE: Bastille Day flare).

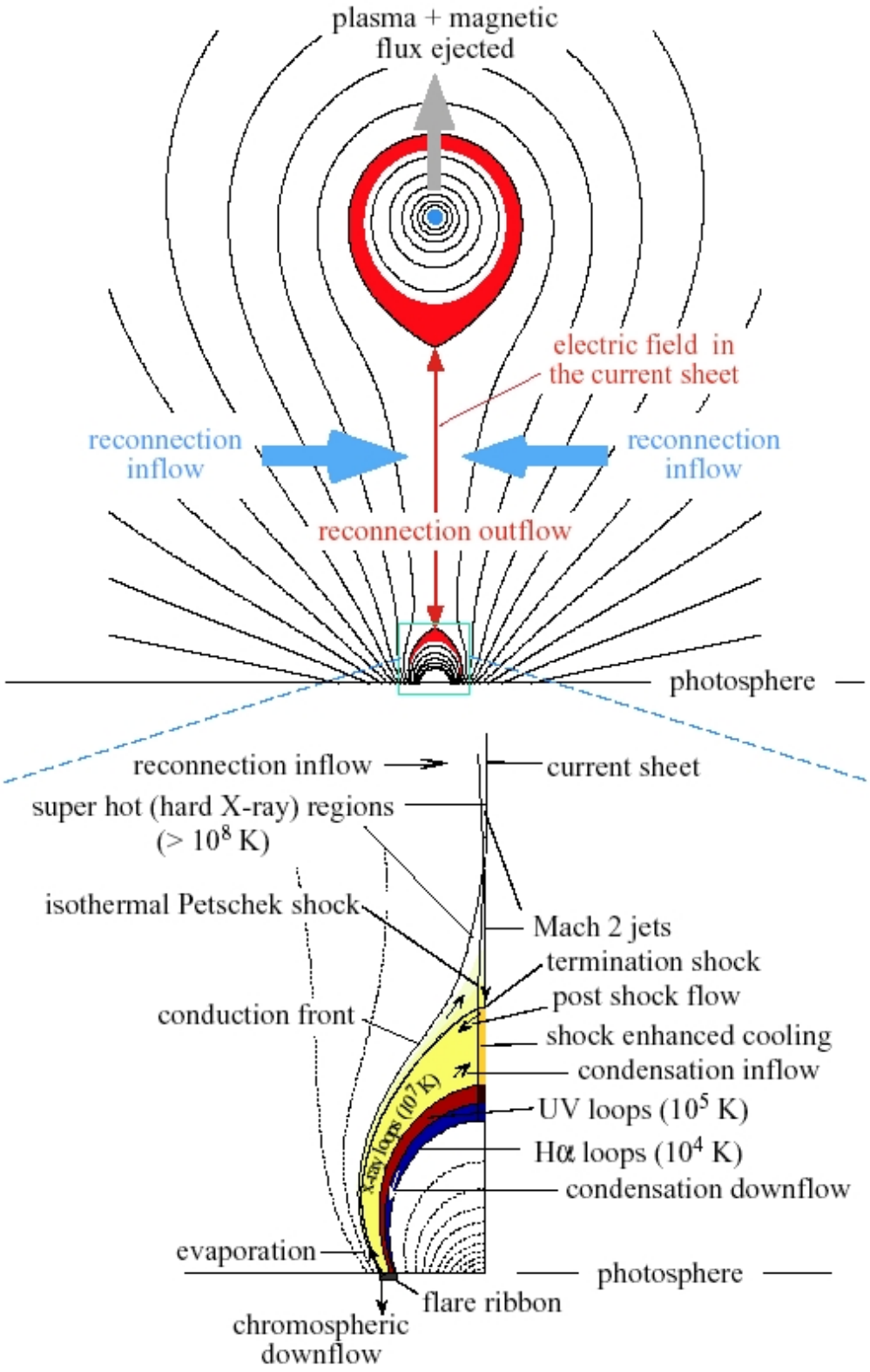

Figure 8.16: A more recent model (CSHKP+) contains many features that are not easily observed, but verified from theoretical considerations (Lin & Forbes 2002).

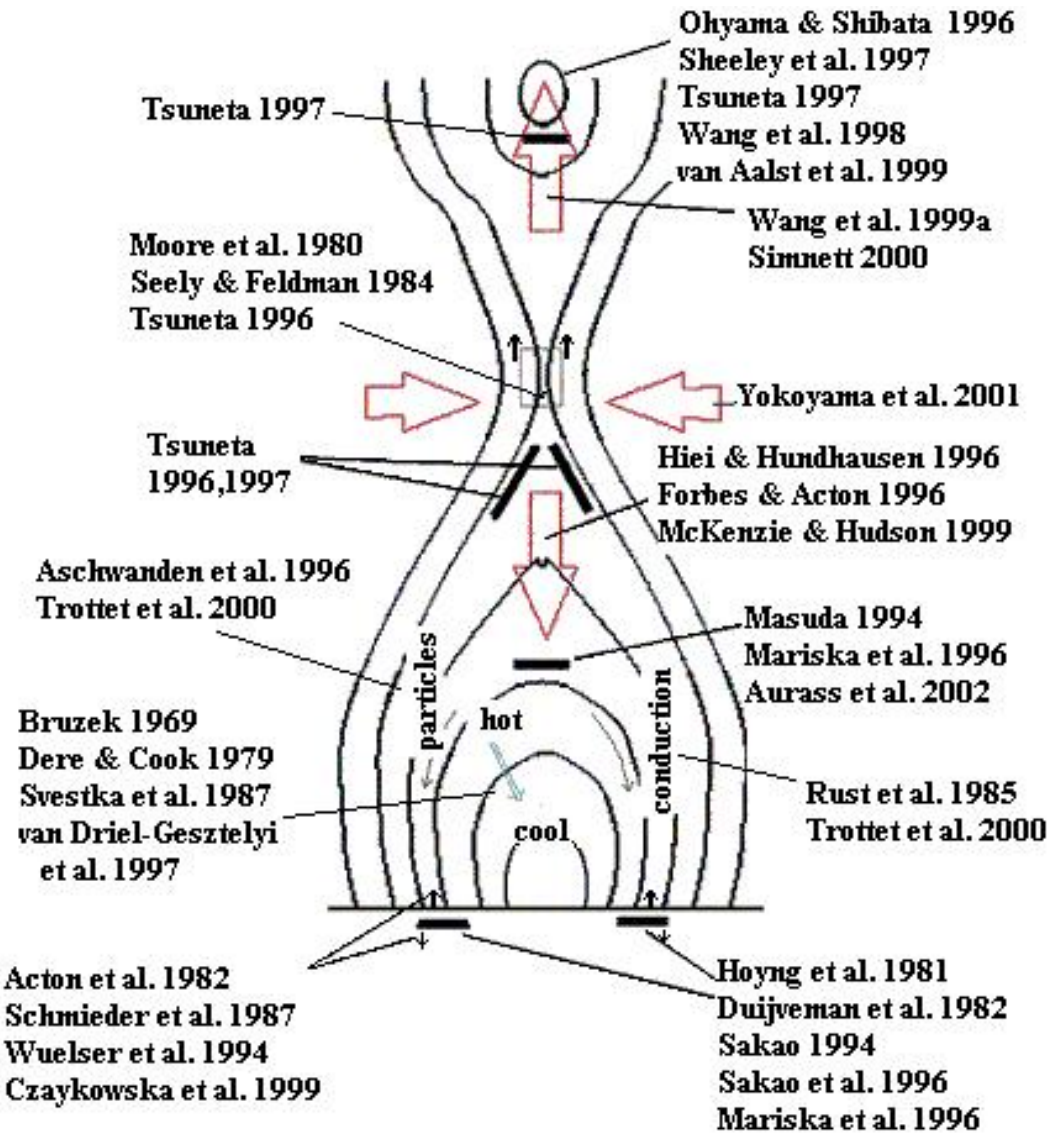

Figure 8.17: A summary of the different models was presented by McKenzie in the 10th Yohkoh Anniversary Meeting in 2001.

8.3 Predictions for activity

Mount Wilson Magnetic Classifications

Alpha: Denotes a unipolar sunspot group

Beta: A sunspot group having both positive and negative magnetic polarities, with a simple and distinct division between the polarities

Gamma: A complex active region in which the positive and negative polarities are so irregularly distributed as to prevent classification as a bipolar group

Delta: A complex magnetic configuration of a sunspot group consisting of opposite polarity umbrae within the same penumbra – **most probable to erupt**

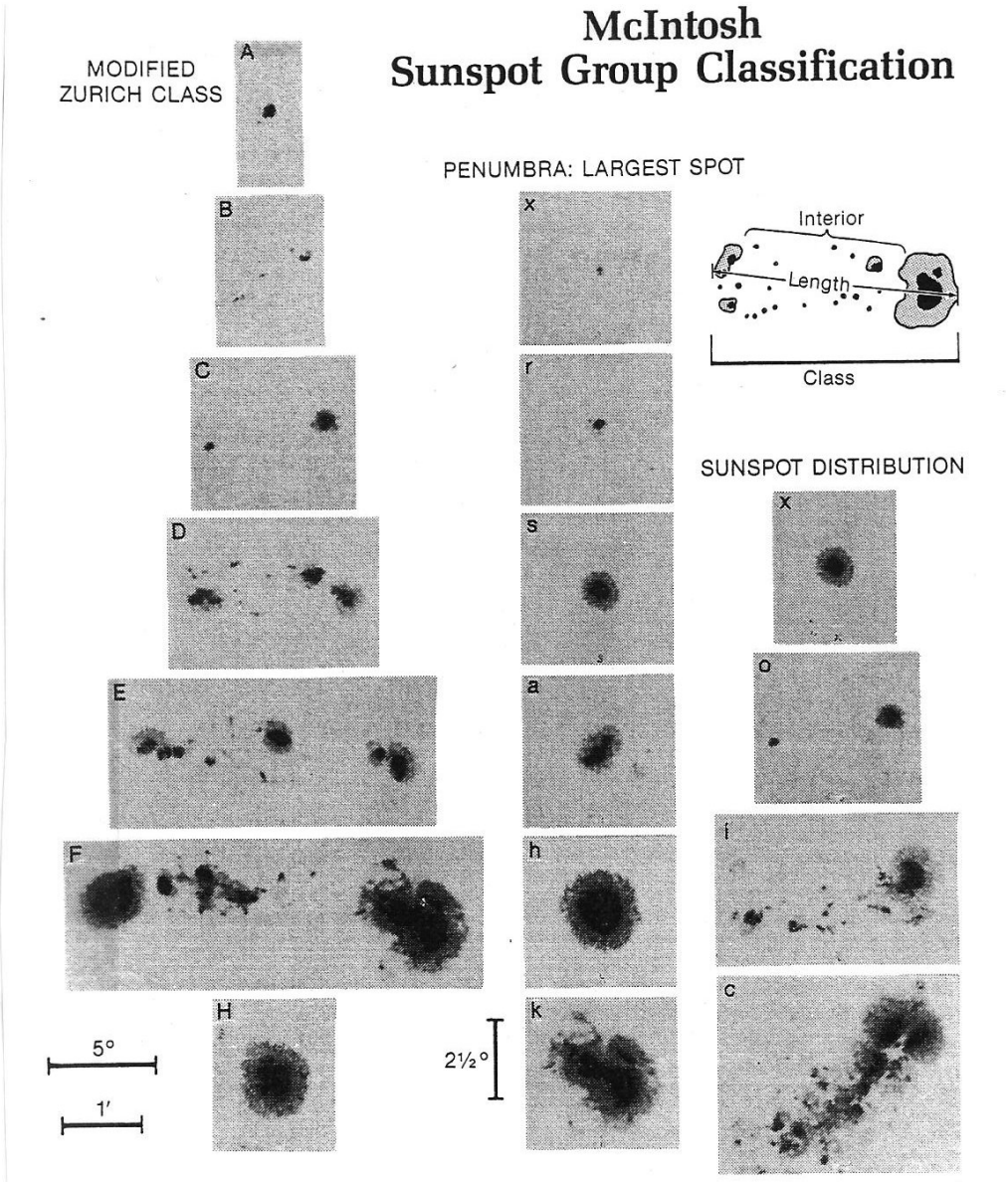

Fig. 6.4 The McIntosh sunspot classification scheme. Three letters describe in turn the class of sunspot group (single, pair or complex group), the penumbra of the largest spot in the group, and the spot distribution. (Courtesy P.S. McIntosh, NOAA (1990))

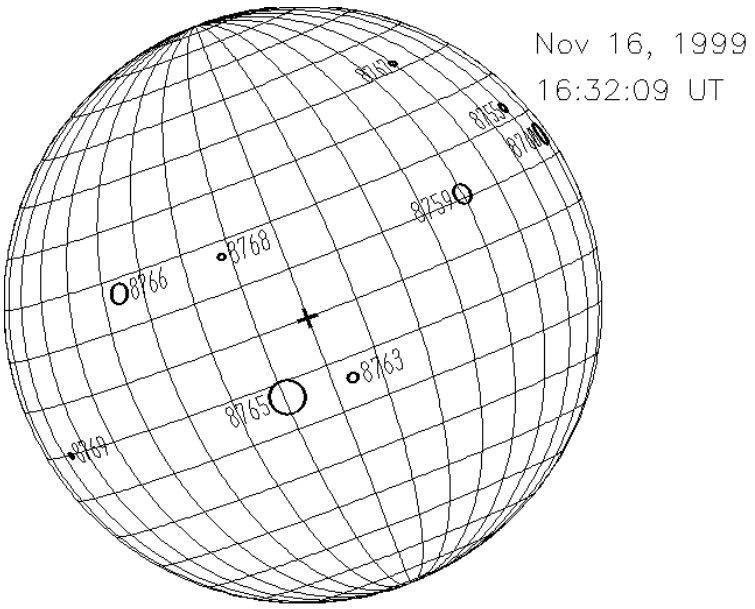

Joint USAF/NOAA Solar Region Summary (NOV 16,1999 00:00:00 UT)

NMBR	LOCATI	LO	AREA	Z	LL	NN	MAG TYPE
8755	N23W61	315	0080	HSX	02	01	ALPHA
8759	N11W32	286	0270	FAI	21	44	BETA-GAMMA
8760	N15W70	324	0420	FKO	17	11	BETA
8763	S14E04	250	0070	CSO	06	07	BETA
8765	S13E19	235	0820	EKC	14	34	BETA-GAMMA
8766	N17E44	210	0270	DKI	07	13	BETA-DELTA
8767	N42W42	296	0040	CSO	05	05	BETA
8768	N17E20	234	0030	DSO	06	07	BETA
8769	S10E76	178	0030	HSX	01	01	ALPHA

Figure 8.18: Sunspot regions are identified with their NOAA number, given by the National Oceanic and Atmospheric Administration, USA. Daily measurements are made of the sunspot group positions, magnetic classification, maximum magnetic field strength, group number, Zurich class, Penumbra class, compactness class, number of spots, longitudinal extend in degrees, total spot areas, individual spot areas, etc.

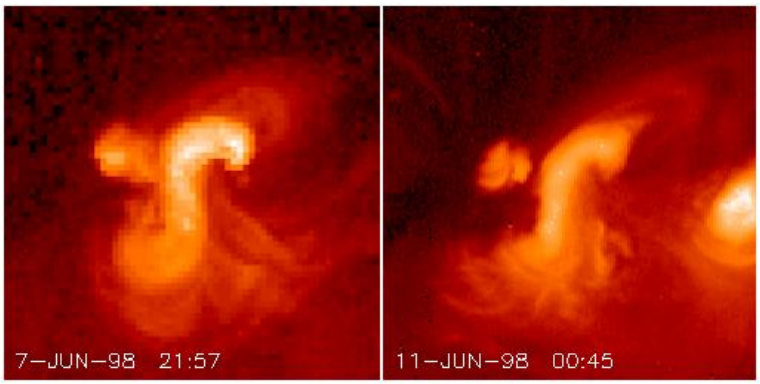

Figure 8.19: Sigmoid (S-shaped) structures in active regions forecast eruptions. However, not all sigmoid regions erupt. (Yohkoh soft X-ray image of a hot, coronal S-shaped region).

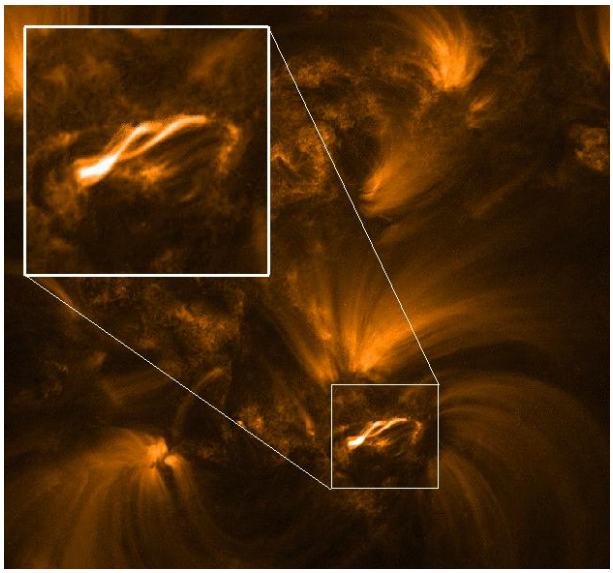

Figure 8.20: Low-lying wrapped loops (TRACE EUV image of chromospheric loops, that are cooler than the coronal soft X-ray loops).

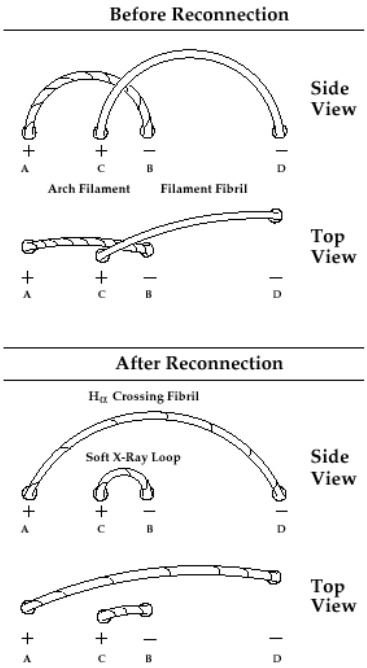

Figure 8.21: Simple reconnection model for wrapped loops. Note that the loops can appear as S-shaped structures when looked from above with instruments that have low spatial resolution (cartoon by Canfield & Reardon, Solar Phys., 1998).

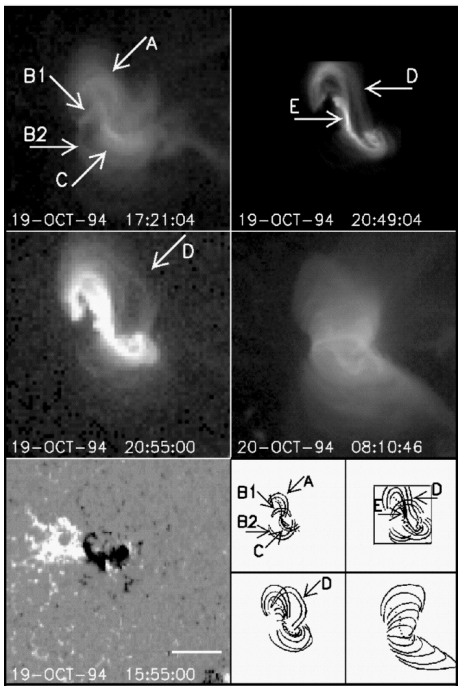

Figure 8.22: Sigmoids often evolve into ejective eruptions (Moore et al. ApJ 552, 2001).

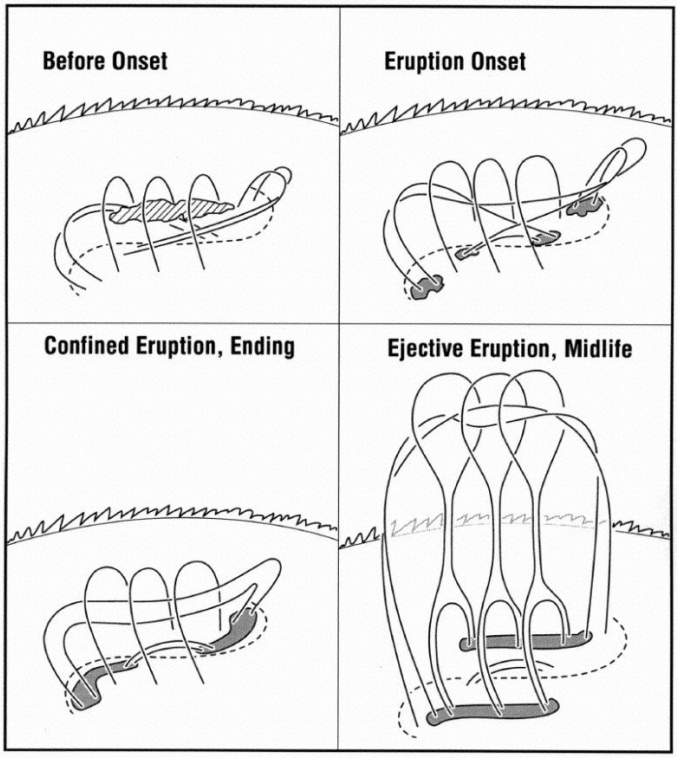

Figure 8.23: The separation between confined and ejective eruptions. Moore et al. (2001) found that 4 out of 6 analysed S-shaped region events were ejective.

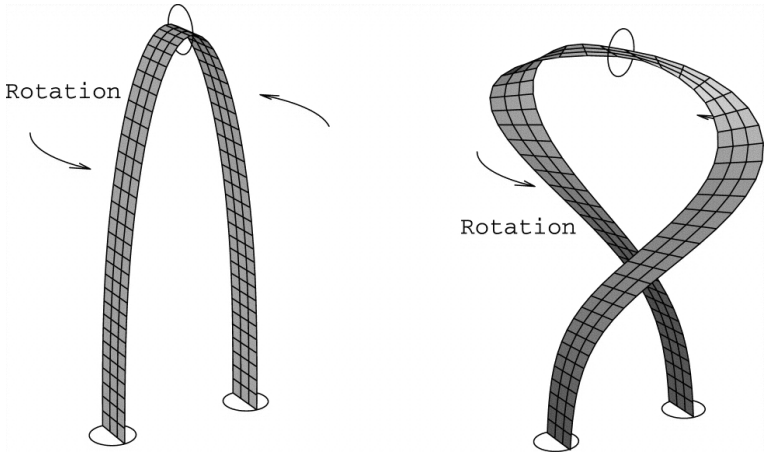

Figure 8.24: Twist and writhe of magnetic flux tubes: Plasma flows, solar rotation, etc. can cause footpoint movement and twisting of loops, that lead to reconnection (Lopez Fuentes et al., 2000).

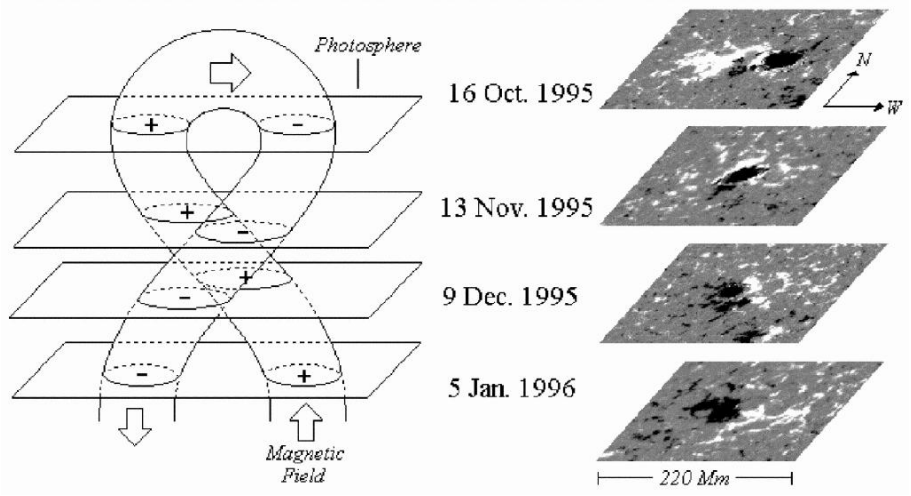

Figure 8.25: Emergence of twisted flux tubes is also possible. The twist will "unfold" during and after emergence, which can be observed as rotating magnetic polarities (see magnetograms on the right; from Lopez Fuentes et al., 2000).

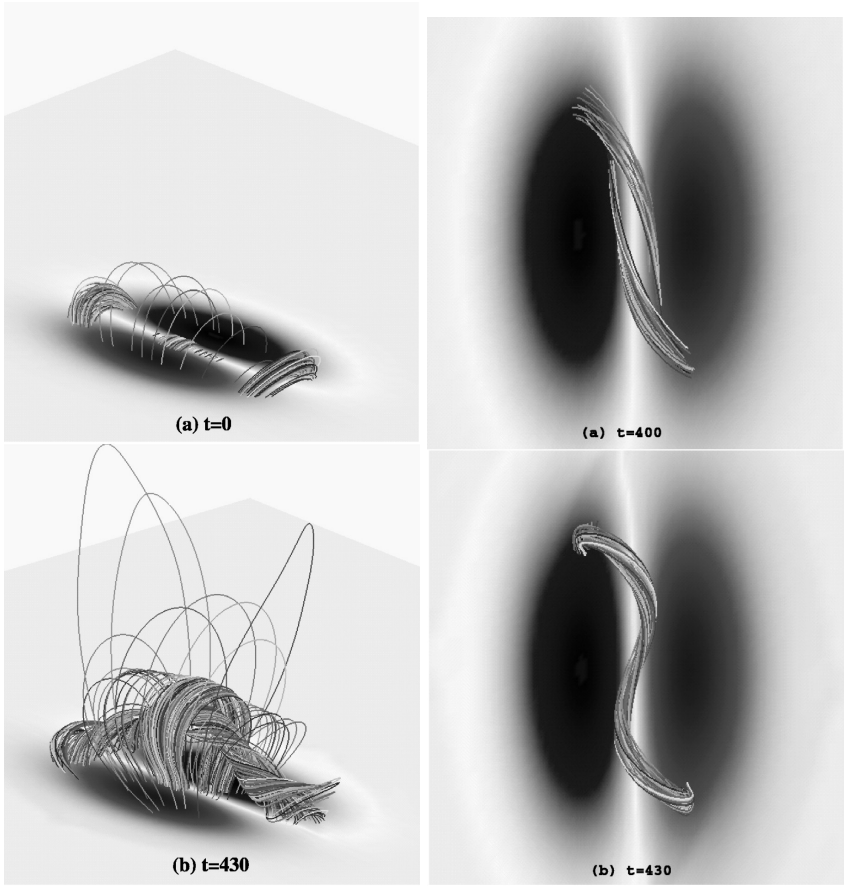

Figure 8.26: MHD simulations of the evolution of an S-shaped region: Selected field lines of the configuration when a twisted flux rope has been created. Top view of selected field lines showing the merging of two inverse J-shaped structures visible at t = 400 into a single inverse S-shaped structure at t = 430.(Amari et al. ApJ, 2000)

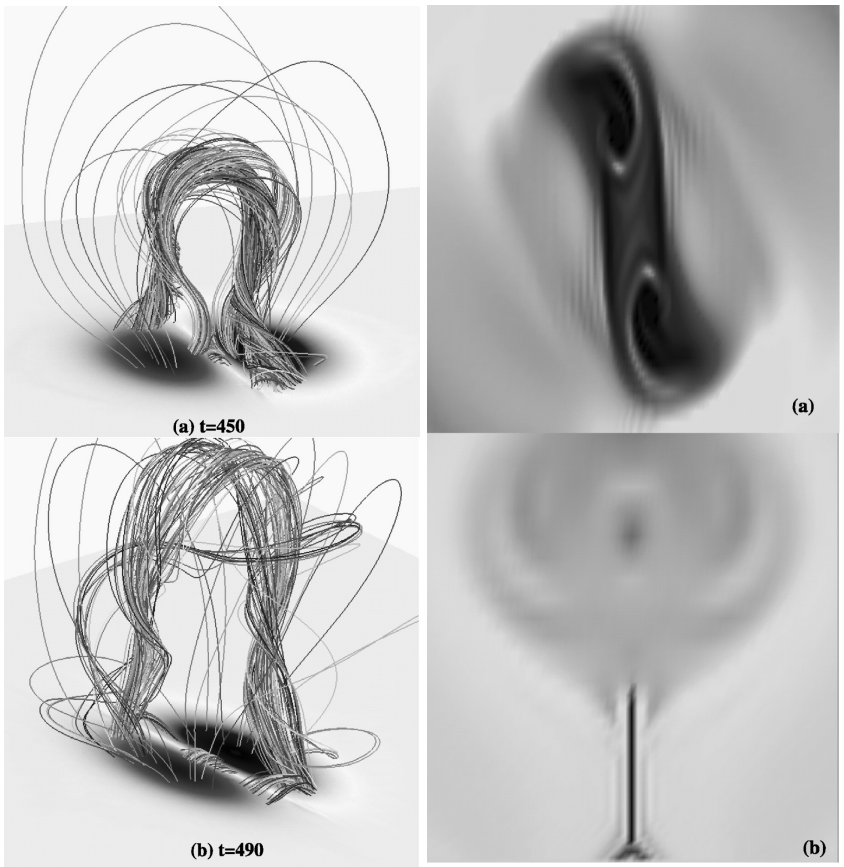

Figure 8.27: For t = 430 the configuration experiences a major global disruption. The twisted flux rope expands very rapidly; evolution of the configuration at two steps during a relaxation phase at t = 450 and t = 490. No neighboring equilibria exist, and the configuration experiences a major disruption. (Amari et al. ApJ, 2000)

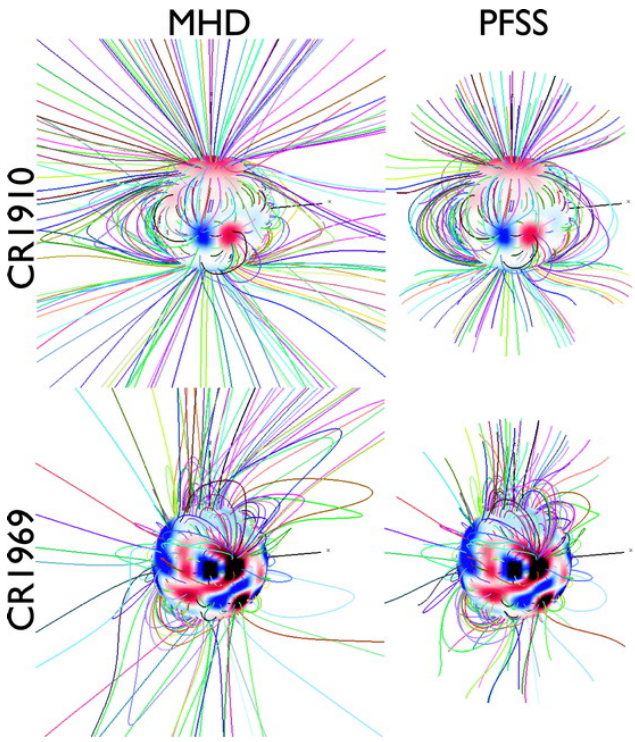

Figure 8.28: Magnetic field extrapolations can be done with the Solarsoft software, using potential field source surface (PFSS) code. PFSS solutions have been found to match MHD results for configurations based on untwisted coronal fields (i.e., when driven by line-of-sight magnetograms). It remains an open question whether MHD solutions will differ more substantially from PFSS solutions when vector magnetograms are used as boundary conditions. This will be addressed in the near future when vector data from the Solar Dynamics Observatory and Hinode become incorporated into the MHD models. (Riley et al., ApJ 653, 2006).

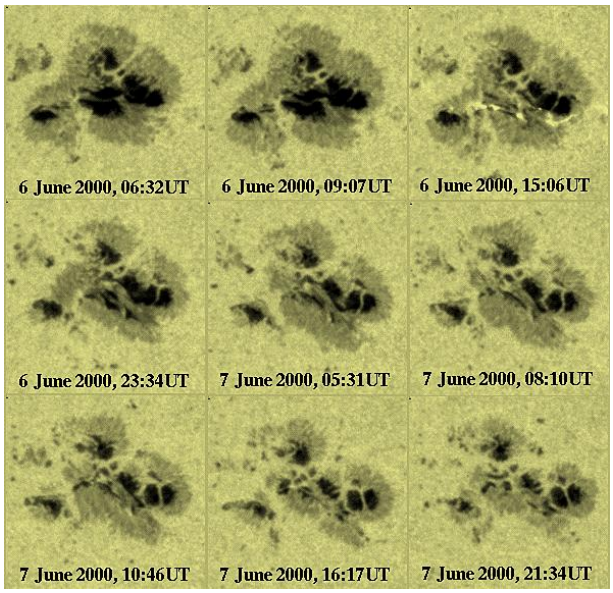

Figure 8.29: Sunspot regions disintegrate within time.

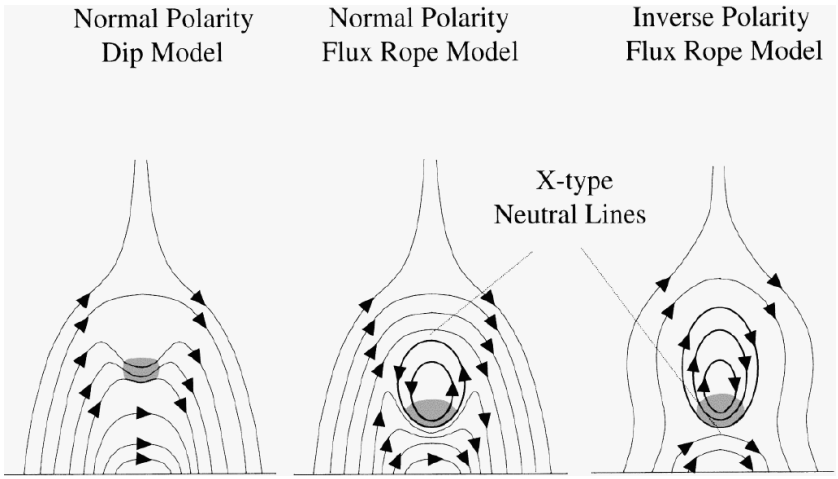

Figure 8.30: Filament support models: Dip model → flux rope model when filament moves downward until reconnection occurs above (X-type neutral line). In inverse polarity model flux rope emerges from below (Gilbert et al. ApJ 537, 2000).

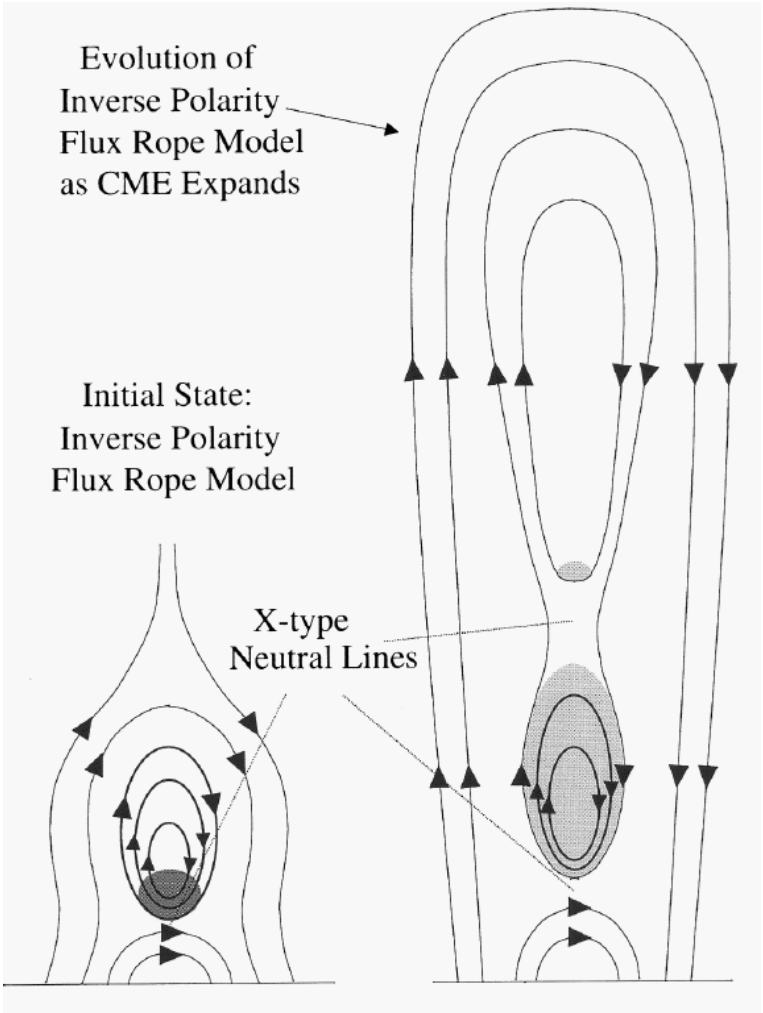

Figure 8.31: Filament eruption model (Gilbert et al. 2000)

8.4 Reconnection models

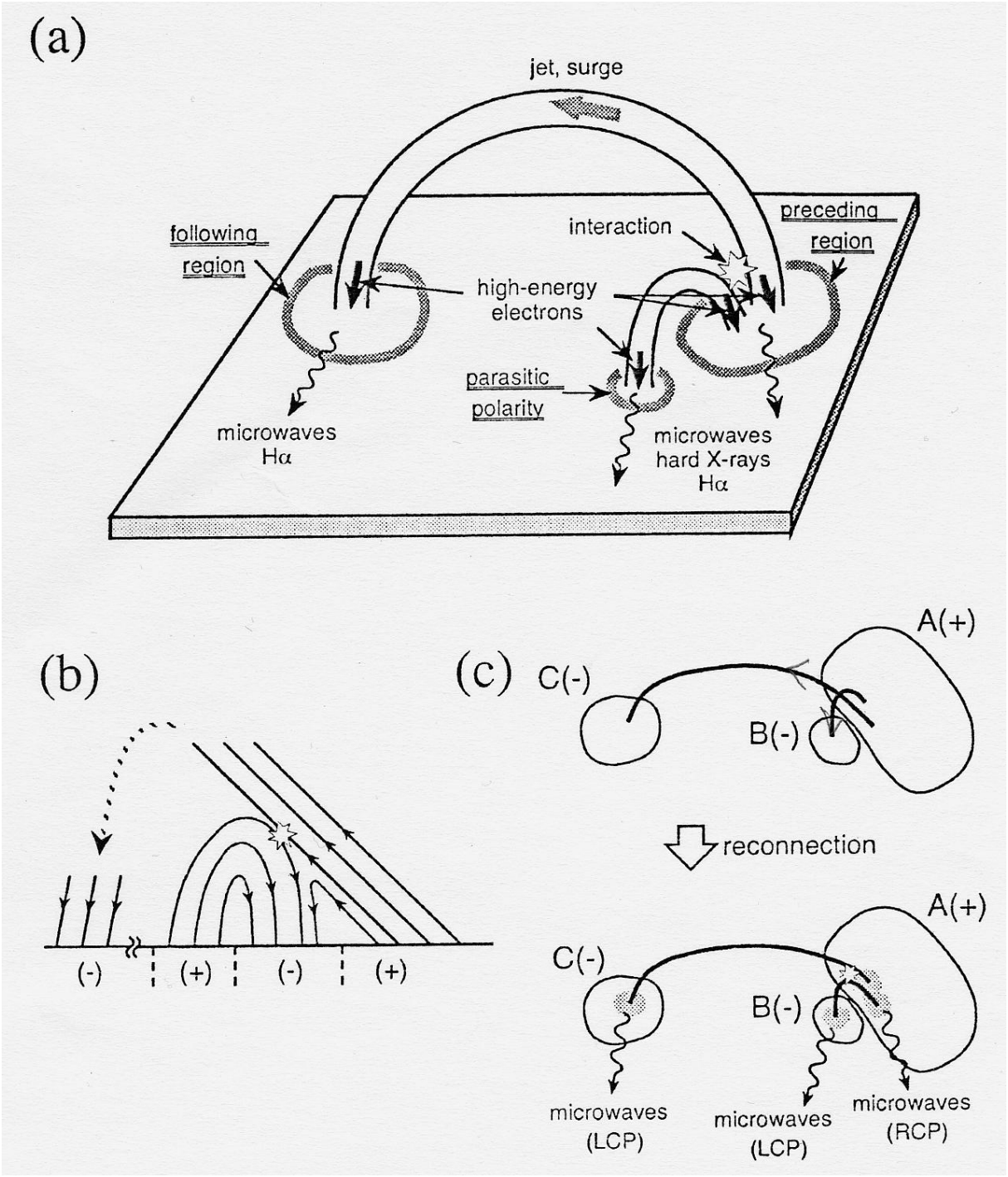

Figure 8.32: Emerging flux is a simple way to cause reconnection: the rising opposite polarity region reconnects with the existing flux and the new loop interacts with the older one that lies above in this plot. Hanaoka (PASJ 51, 1999) shows a schematic drawing of a double-loop flare and behaviour of high-energy electrons. The interaction region of the two loops is the origin of high-energy electrons and thermal plasma flows, such as jets and surges.

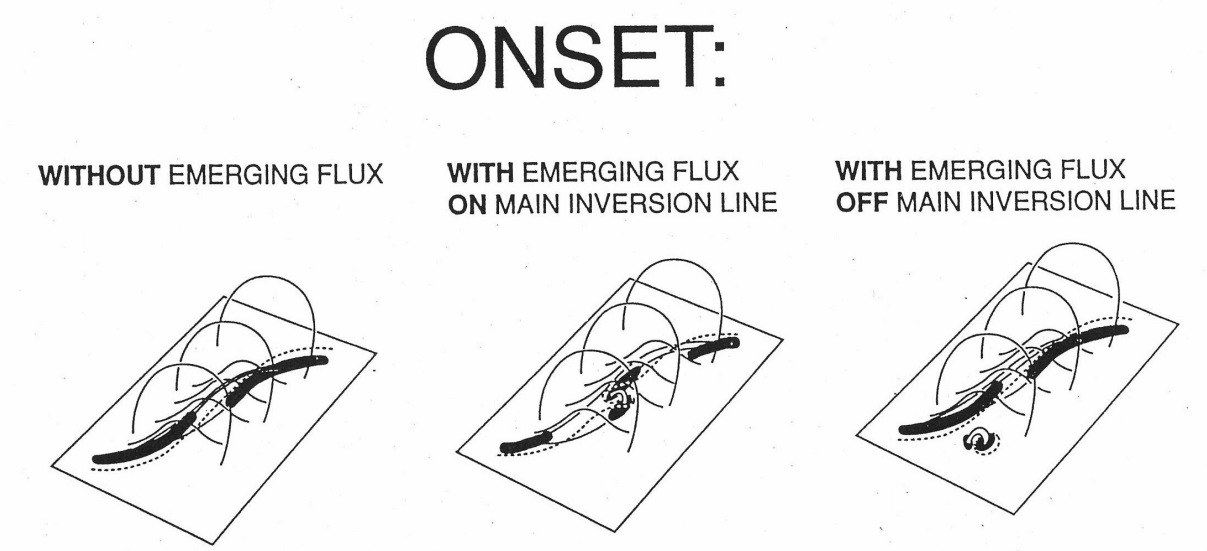

Figure 2. Typical onsets of eruptive flares; left: no emerging flux; center: emerging flux on main inversion line; right: emerging flux off main inversion line. Here, as in Figure 1, the dashed lines are magnetic inversion lines, dividing areas of opposite polarity in the photosphere; black areas are ribbons of chromospheric flare brightening. In all three cases, at flare-ribbon onset the sheared core field along and above the main inversion line has begun to erupt upward, distending the surrounding envelope field, and the initial flare ribbons along the main inversion line are tucked under the erupting core.

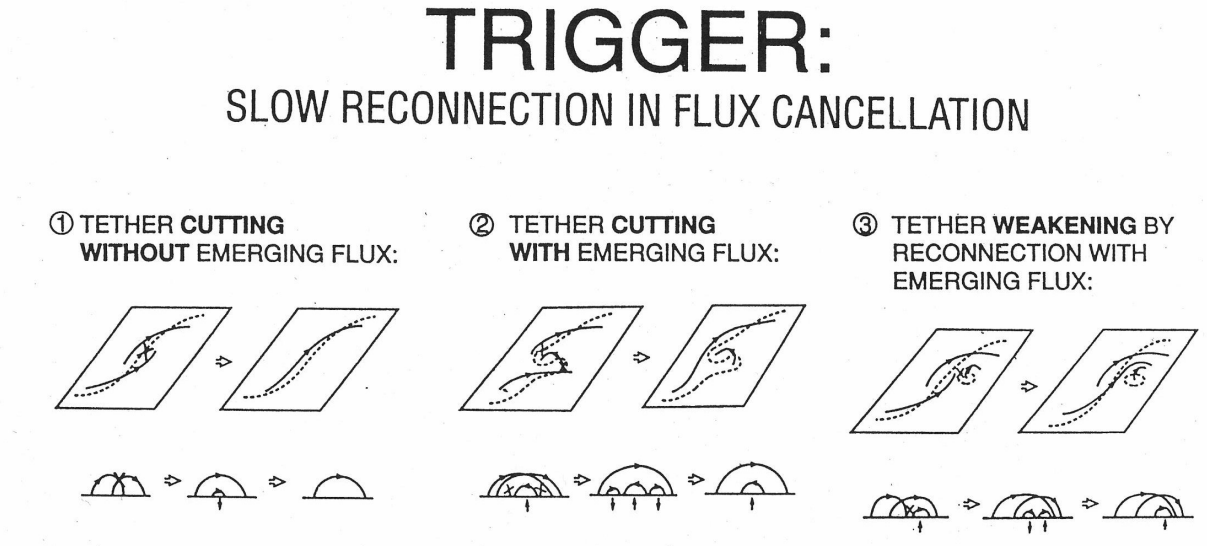

Figure 4. Inferred process for triggering typical onsets of eruptive flares; left: no emerging flux; center; emerging flux on main inversion line; right: emerging flux off main inversion line. The field lines shown are in the core of the preflare field configuration shown in Figures 1-3. The sequences of 2-D sketches below the perspective sketches show the reconnection, emergence, and submergence of field in an end view along the main inversion line. X's mark reconnection. Vertical arrows below the 2-D sketches mark flux emergence (upward arrow) and flux submergence (downward arrow).

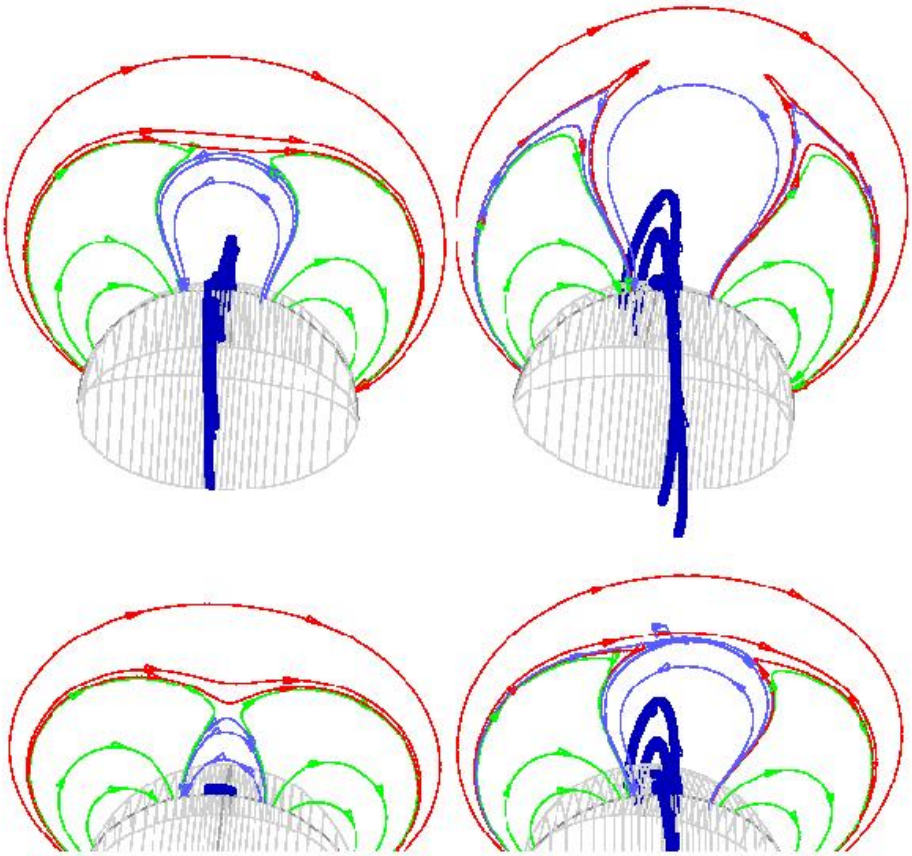

Figure 8.33: Reconnection models: magnetic breakout (Antiochos et al., 1999). A magnetic breakout is the opening of initially low-lying sheared fields, triggered by reconnection at a null point that is located high in the corona and that defines a separatrix enclosing the sheared fields). DeVore & Antiochos (ApJ 628, 2005): In this model, the magnetic free energy that drives the eruption is stored readily in the pre-reconnection state: the energy required to open the stressed flux in the initial configuration can be much greater than that in the post-reconnection state, because more overlying flux must be opened in the former than in the latter. Once the breakout reconnection begins, it accelerates inexorably as the open energy declines, progressively and rapidly. The resultant excess magnetic free energy is converted into kinetic and gravitational energy of the CME plasma, which escapes in an ideal expansion. Subsequently, flare reconnection across the current sheet trailing the ejected flux produces a flux rope and a closed coronal arcade, similar to those in other models. Unlike those scenarios, however, in the breakout model flare reconnection results from, rather than causes, the eruption.

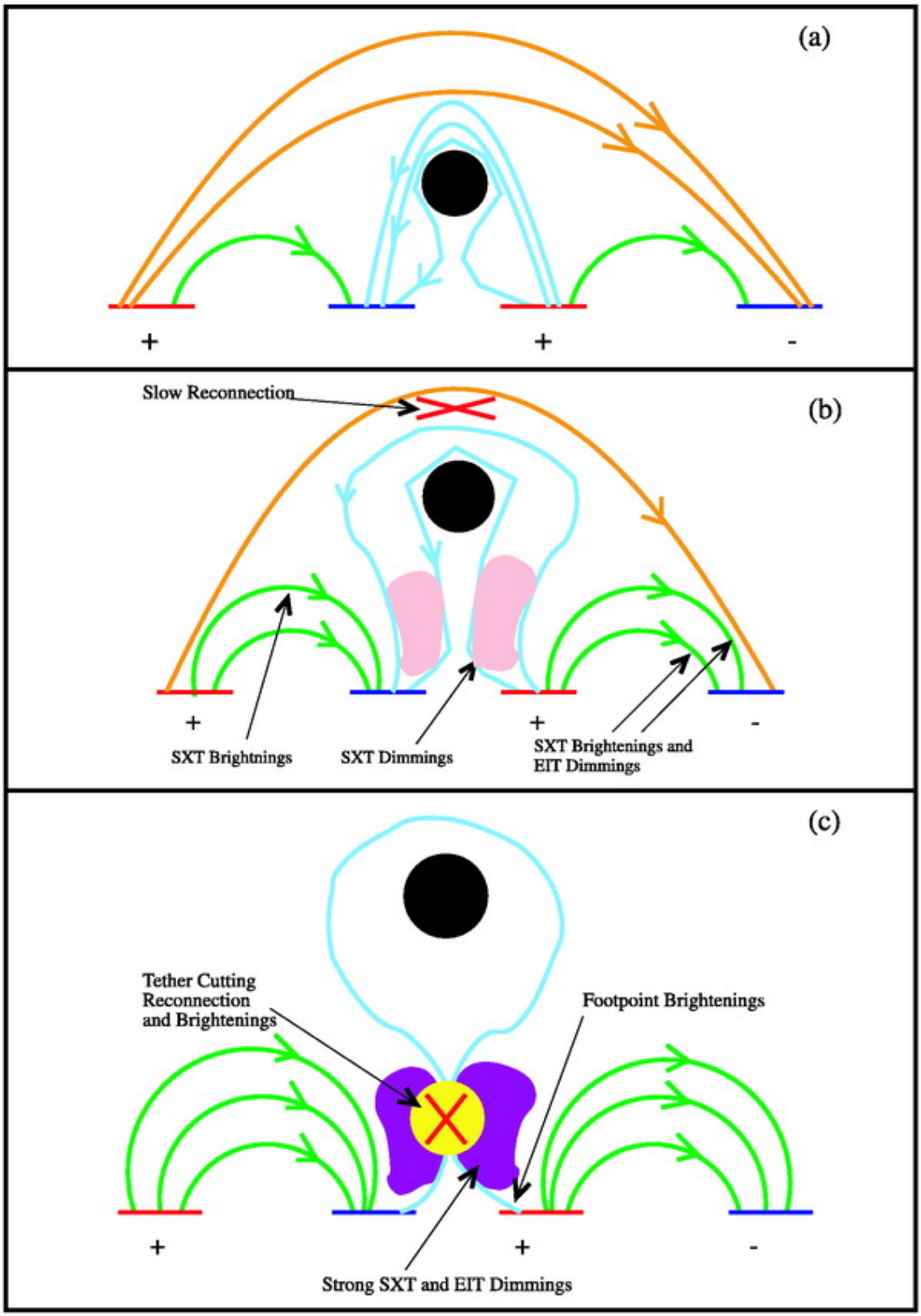

Figure 8.34: Tether cutting + breakout (Sterling & Moore 2004).

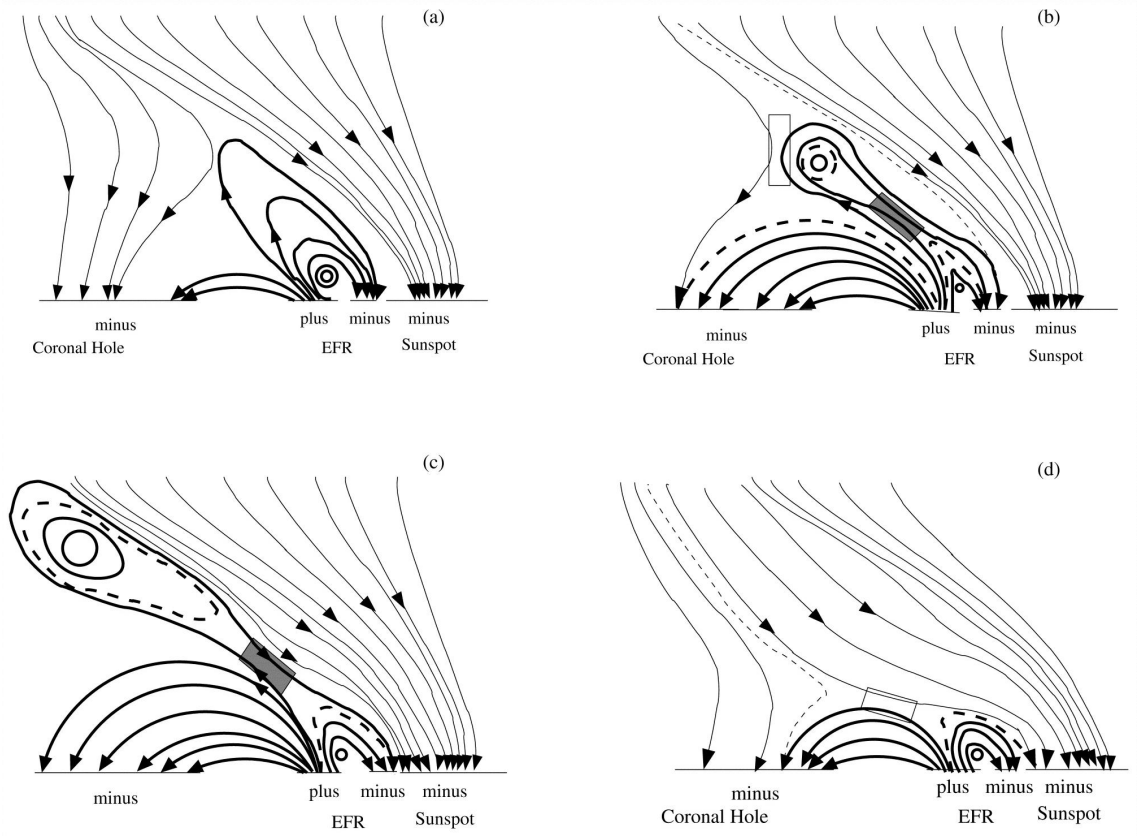

Figure 8.35: Emerging flux region (EFR) meets coronal hole field lines and creates outer reconnection, followed by inner reconnection (Sterling et al. 2001).

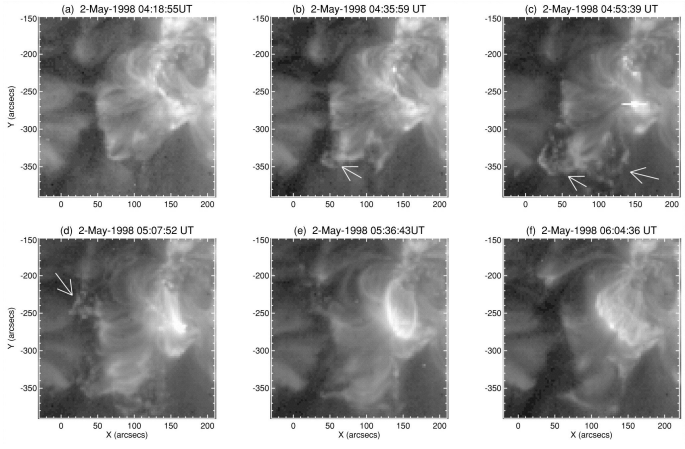

Figure 8.36: EIT crinkles would then be caused by the heated plasma and enhanced density region that is pushed toward the coronal hole (Sterling et al. 2001).

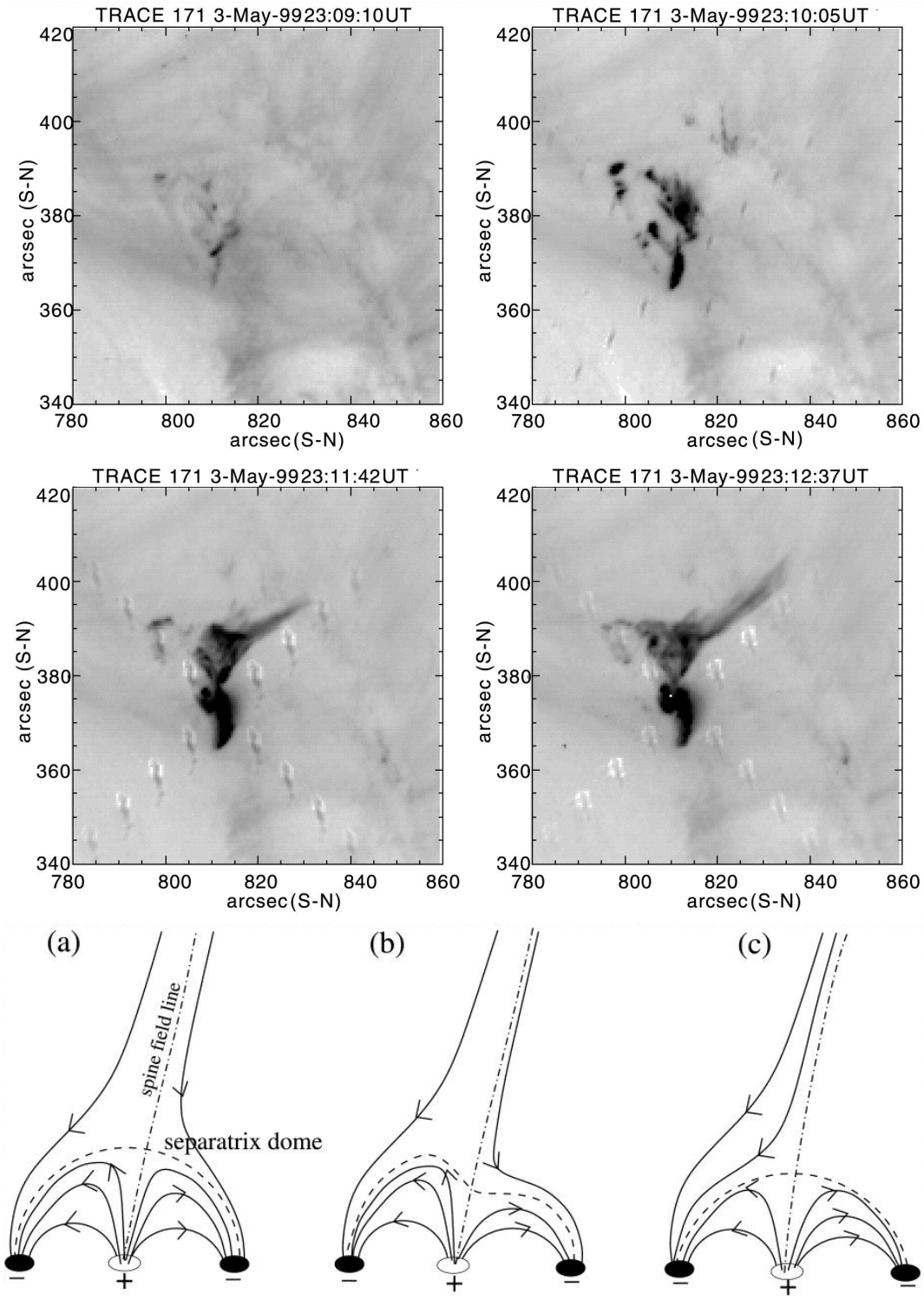

Figure 8.37: Creation of plasma jets: TRACE 171 Å images of the flare site made around the impulsive phase. Near the time of the HXR impulsive phase the TRACE emission is confined to a few bright kernels; shortly thereafter, the kernels disappear, a small loop brightens, and material ejection starts. Two-dimensional representation of the process of reconnection via a separator dome (Fletcher et al. Astrophysical Journal, 2001)

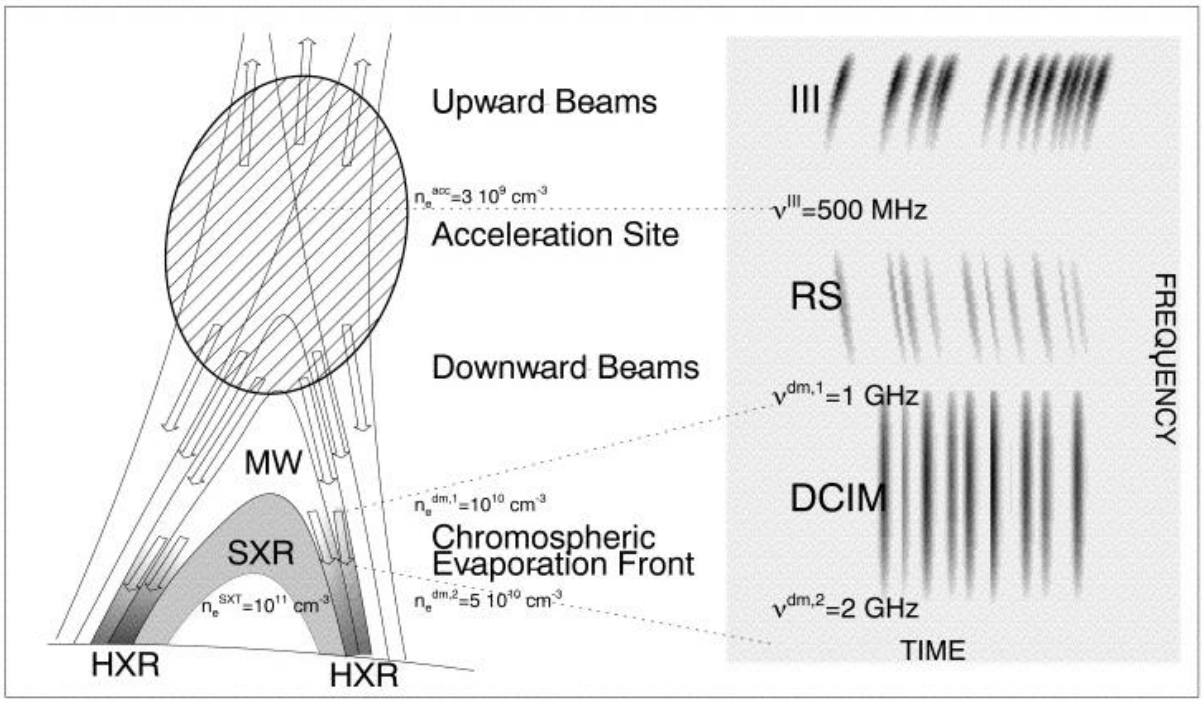

Figure 8.38: Diagram of a flare model envisioning magnetic reconnection and chromospheric evaporation processes in the context of electron density measurements. The panel on the right illustrates a dynamic radio spectrum with radio bursts indicated in the frequency-time plane. The acceleration site is located in a low-density region (in the cusp), from where electron beams are accelerated in upward (type III) and downward (RS bursts) directions (Aschwanden & Benz, ApJ 480, 1997).

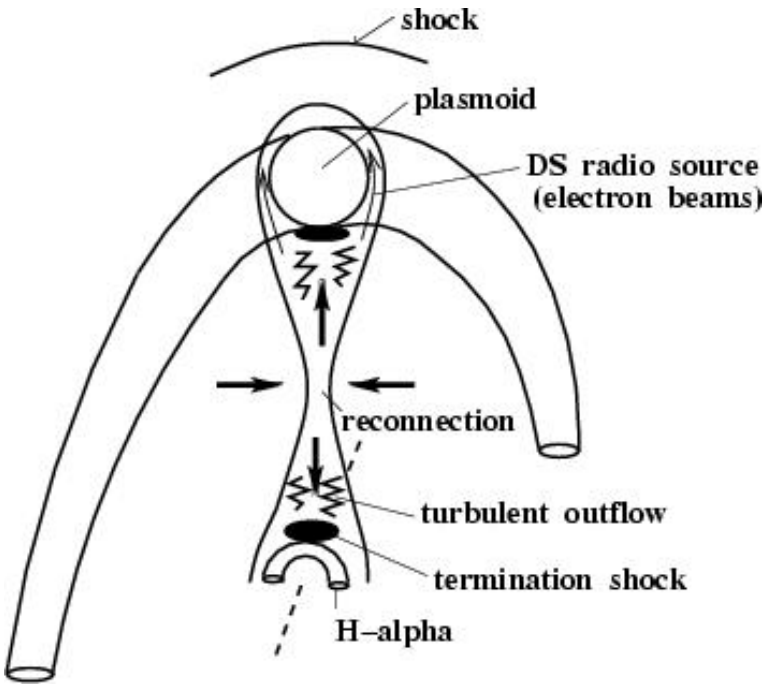

Figure 8.39: Decimetric radio sources (Karlicky, 2004).

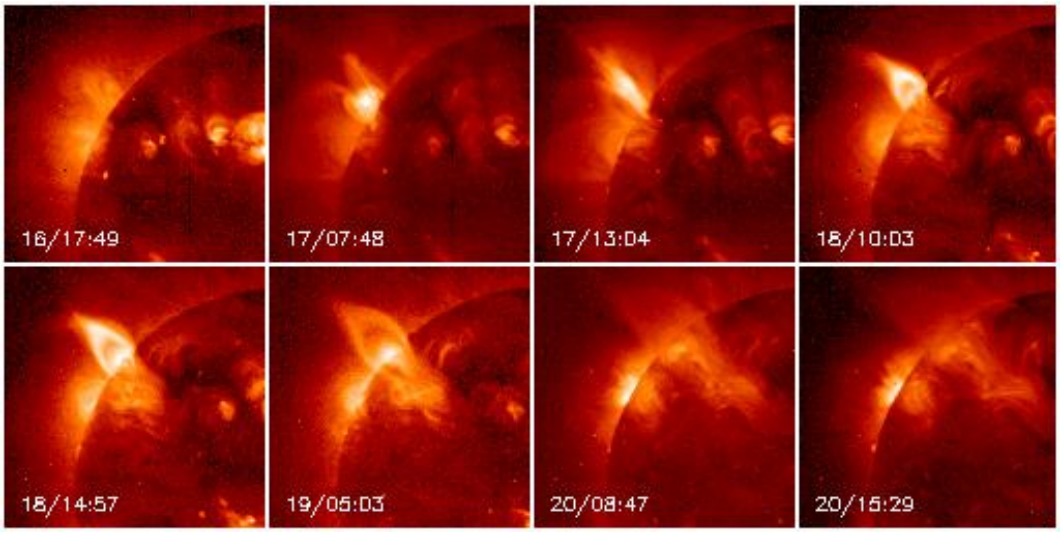

Figure 8.40: Long duration cusp-like sources - no reconnection?

8.5 Accelerated particles

The basic principle of the thick-target model is that the observed hard X-rays result from bremsstrahlung emitted by a beam of electrons accelerated in the corona, but then "precipitating" into the dense atmosphere where they stop collisionally (via Coulomb collisions). The term "thick target" describes just this property of collisional termination of a particle beam. The resulting X-ray spectrum has a fixed dependence on the beam properties. That simplification is one of the model's virtues, permitting an easy use of inverse theory to learn about the (assumed) electron beam. (See more from the RHESSI Science Nugget by Lyndsay Fletcher and Hugh Hudson, at http://sprg.ssl.berkeley.edu/~tohban/nuggets/?page=article&article_id=44)

- Thick target: Double-footpoint, need 10^{37} electrons per second to explain the HXR emission (typical loop 10^{37} electrons!)
- Thin target: Superhot thermal source > 10^8 K (Masuda-flare)

HXR thin target – thick target

$$E^{\delta_{thin}}: \quad \delta_{thin} = \gamma - 0.5 \tag{8.1}$$

$$E^{\delta_{thick}}: \quad \delta_{thick} = \gamma + 1 \tag{8.2}$$

where γ is the photon power-law index (Brown, 1971).

Practical example:
observed photons with ϵ = 70 keV → mean energy of electrons
E_x thin-target = 100–130 keV
E_x thick-target = 120-180 keV

Comparison:
Outstreaming electrons in type III bursts have velocities between 0.1c and 0.5c, meaning subrelativistic electron energies of 2–80 keV.

Gyrosynchrotron radio – HXR

$$N(E) \propto E^{-x} \qquad \text{Electron energy spectrum} \tag{8.3}$$

$$I(\nu) \propto \nu^{\alpha_r} \propto \nu^{-(x-1)/2} \qquad \text{Gyrosynchrotron radiation} \tag{8.4}$$

$$N_x(\epsilon) \propto \epsilon^{\alpha_x} \propto \epsilon^{-(x+1/2)} \qquad \text{X-ray emission} \tag{8.5}$$

$$\alpha_r = 0.5\alpha_x - 0.75 \tag{8.6}$$

These are general relations – no model assumptions, gyrosynchrotron is optically thin, no directional effects assumed (Longair: High-energy Astrophysics)

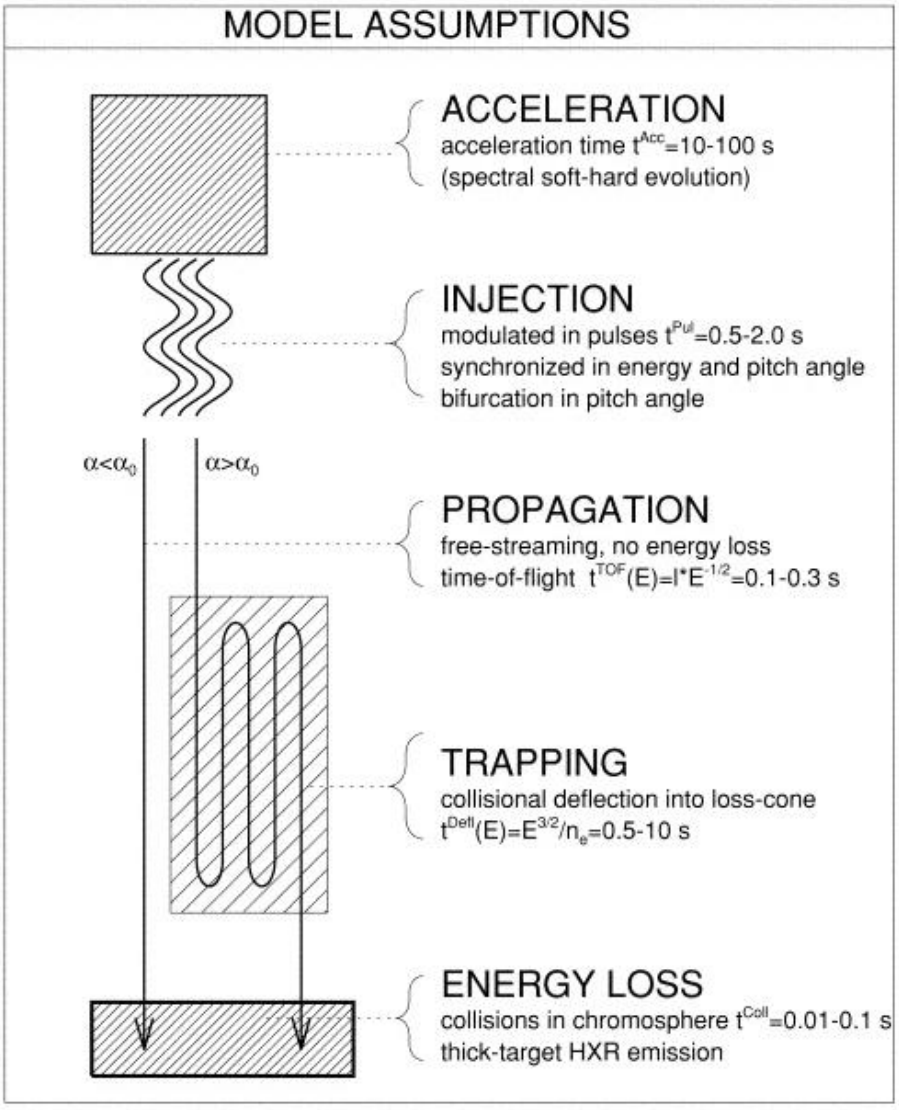

Figure 8.41: Summary of model assumptions used in the deconvolution method of hard X-ray time profiles (Aschwanden, 1998)

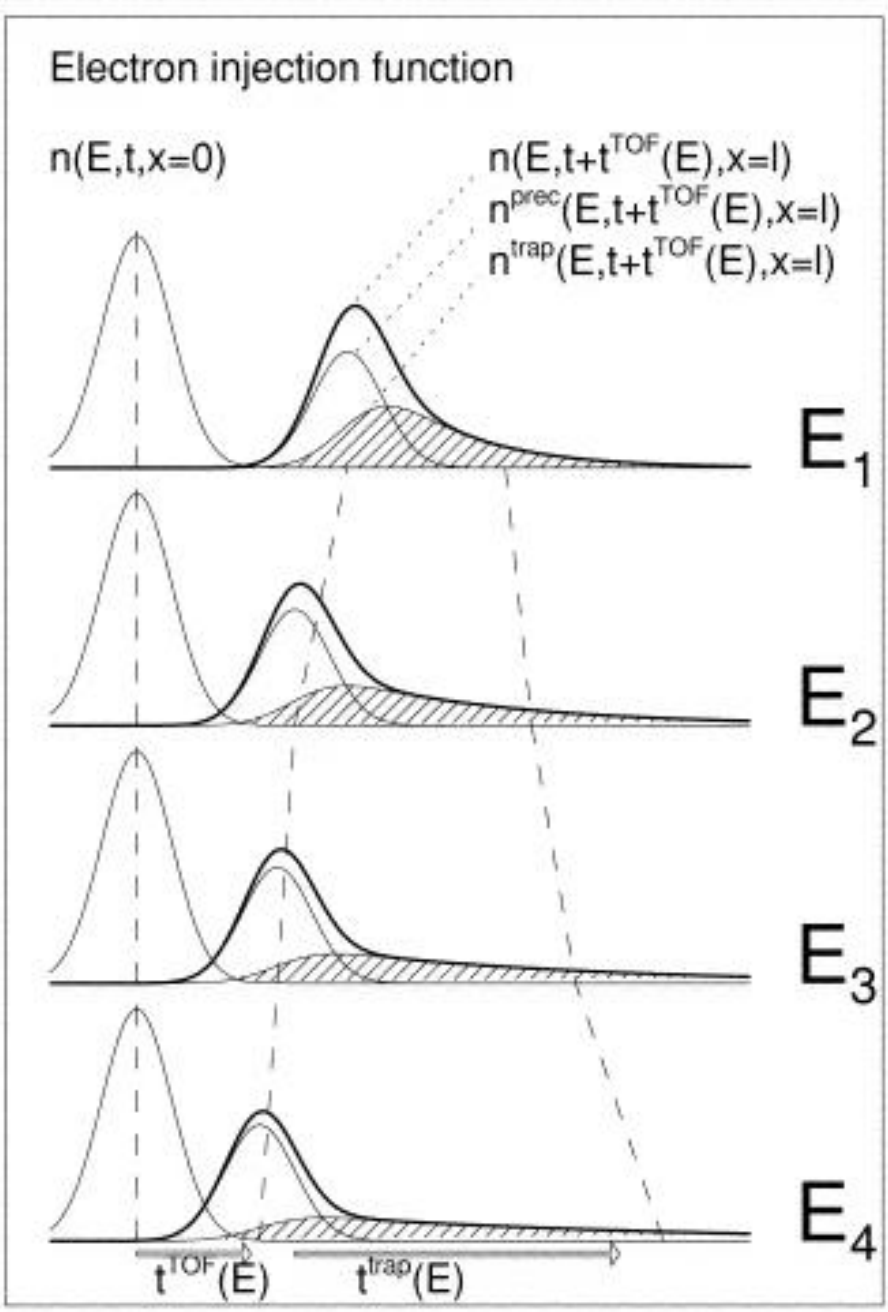

Figure 8.42: Temporal relation of the electron injection function n(E,t,x=0) at the injection site and at the HXR emission site n(E,t + t^{TOF}(E), x = l^{TOF}), delayed by an energy-dependent electron time-of-flight interval t^{TOF}(E), schematically shown for four different energies E1 < E2 < E3 < E4. The injection function at the HXR emission site (thick curve) is broken down into a directly precipitating component (thin curve) and the trap-precipitating component (hatched area). Note that the (e-folding) trapping time t^{trap}(E) increases with energy E, whereas the time-of-flight delays t^{TOF}(E) decreases.

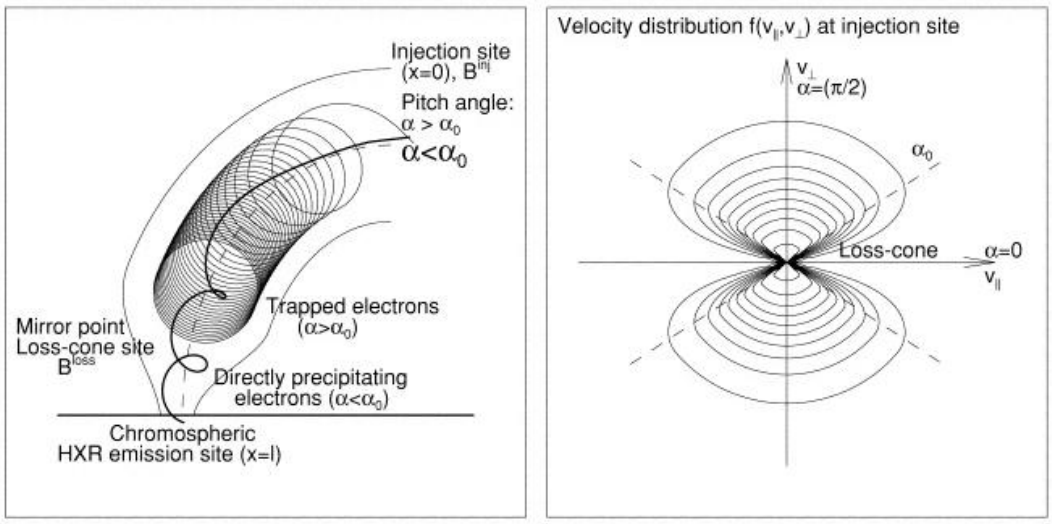

Figure 8.43: Spatial configuration of injection site, loss cone site, and HXR emission site in a flare loop. Electrons with small initial pitch angles precipitate directly, while electrons with large pitch angles become temporarily trapped. Right: The velocity distribution at the injection site has a loss cone for pitch angles $\alpha \leq \alpha_0$.(Aschwanden, ApJ 1998)

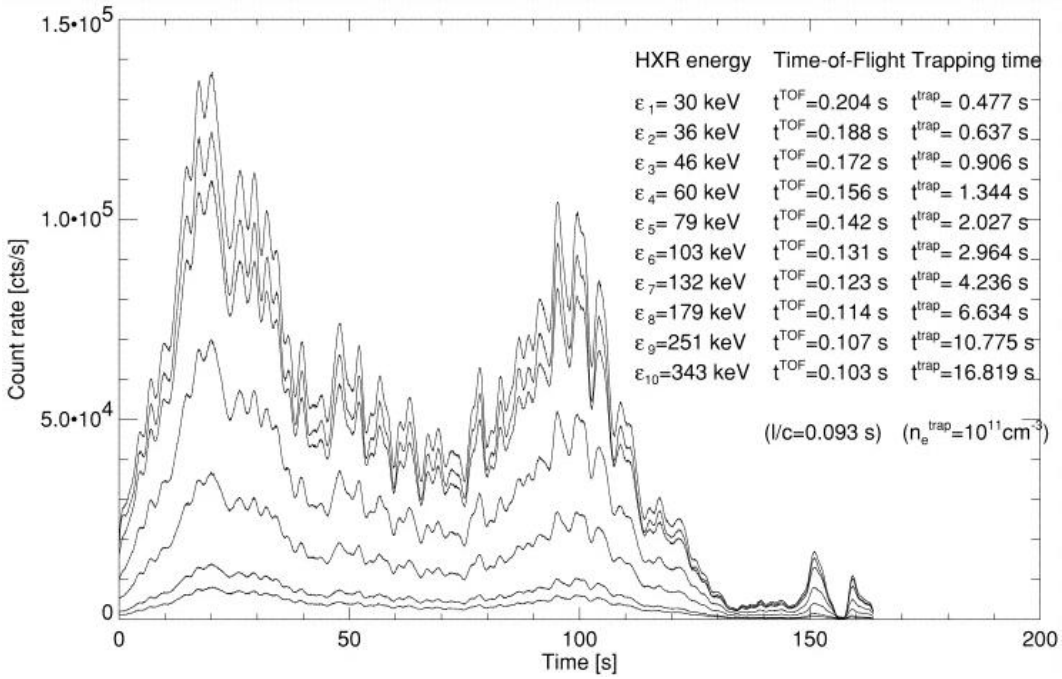

Figure 8.44: Simulated data set of HXR time profiles I(ϵ, t) for 10 energy channels (ϵ_i, i = 1,..., 10). The first channel is taken from observed BATSE/MER count rates of the solar flare 1991 November 13, 21:15:55 UT, while the time profiles of the other channels were convolved with TOF delays (occurring over a projected distance of l = 15,000 km) and trap delays (based on collisional deflection times in a plasma with an electron density of $n_e = 10^{11}\text{cm}^{-3}$). The fluences of all channels are scaled proportionally to the fluences of the observed BATSE/MER channels. Data noise on timescales of 1 s has been filtered out with a Fourier filter.